To the Graduate Council:

I am submitting herewith a dissertation written by Donald W. Roberds entitled "Electronic Instrumentation for Interferometric Particle Sizing." I recommend that it be accepted in partial fulfillment of the requirements for the degree of Doctor of Philosophy, with a major in Electrical Engineering.

E. C. Huebschmann, Major Professor

We have read this dissertation
and recommend its acceptance:

Accepted for the Council:

Vice Chancellor
Graduate Studies and Research

DOE
TID
4624
cop. 2

ELECTRONIC INSTRUMENTATION FOR INTERFEROMETRIC PARTICLE SIZING

A Dissertation

Presented for the

Doctor of Philosophy

Degree

The University of Tennessee

Donald W. Roberds

December 1975

1269166

ACKNOWLEDGMENTS

The author is indebted to a number of people for their assistance in the course of this work. Discussions with members of Advanced Concepts of ARO, Inc., helped to clarify a number of points pertaining to the theory presented; in particular, those with B. W. Bomar, R. W. Menzel, H. T. Bentley, Dr. R. A. Belz and Dr. W. M. Farmer (now with Spectron Development Laboratories) were most helpful. The author would like to express gratitude to A. E. Lennert, Branch Manager of Advanced Concepts, without whose support and encouragement the work could not have been done. K. R. Kneile of Central Data Processing provided assistance in the numerical analysis.

The author is particularly indebted to his advisor, Dr. E. C. Huebschmann, for his direction and suggestions during the course of the study. Special appreciation is offered to Carol Elder for her help in preparing the manuscript, and to Judy Wright for her careful typing of the final copy.

The work reported herein was supported by Headquarters, Arnold Engineering Development Center, Arnold Air Force Station, Tennessee, within the terms of Contract F40600-75-C-0004 with ARO, Inc., under Project B34P-12A and was sponsored by the U.S. Army Tank-Automotive Command,

Propulsion Systems Laboratory, Warren, Michigan. Further reproduction is authorized to satisfy the needs of the U.S. Government.

ABSTRACT

The theory of interferometric particle sizing is reviewed. The visibility of the waveform of light scattered from a small particle crossing interference fringes created by two crossed laser beams is discussed, and the relation of the visibility to the particle diameter is derived using scalar diffraction theory. The scattered light waveform and its visibility are analyzed in both the time and frequency domains.

An electronic signal processor was designed and tested to measure the waveform visibility. The processor was designed to work with a dual scatter laser velocimeter having a Bragg cell driven at 15 MHz. The instrument uses electronic aperturing of the probe volume to accept for measurement only those particles passing through or near the center of the probe volume. Results of experimental data indicate the visibility can be measured with an accuracy of 5 percent.

TABLE OF CONTENTS

CHAPTER		PAGE
I.	INTRODUCTION AND BACKGROUND	1
	Introduction	1
	Light Scattering Methods of Particle Sizing	2
II.	INTERFEROMETRIC PARTICLE SIZE ANALYSIS: RELATION OF VISIBILITY TO PARTICLE SIZE	8
	Intensity Distribution in the Probe Volume	8
	Relation of Visibility to Particle Size: Fringe Model	16
	Relation of Visibility to Particle Size: Scalar Diffraction Theory	22
III.	ELECTRONIC METHODS OF VISIBILITY MEASUREMENT	35
	Introduction	35
	Optically Apertured System: Peak Detectors	36
	Optically Apertured System: Integrators	39
	Electronically Apertured System	42
	Visibility Change During Particle Traversal	45
IV.	FREQUENCY ANALYSIS	48
	Time Domain	48
	Frequency Domain	50
V.	SIGNAL PROCESSOR FOR VISIBILITY MEASUREMENT	56
	Signal Bandwidths	56
	Signal Processing Circuit	58
	Control Circuit	71

CHAPTER PAGE

VI. SIGNAL PROCESSOR: BENCH CHECK 90

Linearity and Divider Error 90

Equalizing Channel Time Delays 94

Bias Stability 94

Frequency Response: Signal Circuit 95

Frequency Response: Control Circuit 96

Dynamic Range of Input Signal Amplitudes . . . 97

Total Gain 98

Data Repetition Rate 98

VII. NOISE 100

Thermal Noise and First Stage Amplification Noise 100

Photodetector Shot Noise 103

Laser Fluctuation Noise 109

Summary 110

VIII. EXPERIMENTAL RESULTS 112

Examination of Intensity Distribution in Probe Volume 112

Testing Control Circuit Operation 116

Testing Processor Accuracy of Visibility Measurement 118

Visibility Measurement for Spheres of Known Size 124

Noise 126

IX. CONCLUSIONS 133

CHAPTER PAGE

BIBLIOGRAPHY 137

VITA 141

LIST OF FIGURES

FIGURE		PAGE
1.	Optical Arrangement for Generating a Set of Interference Fringes	9
2.	Geometry for Two Crossed Laser Beams, $\vec{K}_1$ and $\vec{K}_2$	11
3.	Intensity Distribution in the Probe Volume	14
4.	Scattered Intensity for Three Values of D/δ, $z = 0$	17
5.	Theoretical Curves of Visibility V_0 Versus Ratio of Diameter to Fringe Spacing D/δ	23
6.	Diffraction Geometry	29
7.	Visibility Measurement Using Peak Detectors	38
8.	Visibility Measurement Using Integrators	40
9.	Visibility Measurement with Electronic Aperturing of the Probe Volume	44
10.	Frequency Spectra: Pedestal and A.C. for $z_n = 0$, 1.0; Visibility for $z_n = 0.25$	53
11.	Signal Processing Circuit, Part I	59
12.	A.C. Envelope Detector Response	63
13.	Signal Processing Circuit, Part II	68
14.	Control Circuit, Part I	75
15.	Control Circuit, Part II	80
16.	Output Versus Input Visibility for Envelope Detector/Divider Combination	93

FIGURE PAGE

17. Scattered Light and Processor Waveforms for Three Values of z_n 114

18. Control Circuit Operation 117

19. Scattered Light Waveforms and Corresponding Processor Output Visibility 119

20. Processor Output Visibility Versus Input Waveform Visibility 121

21. Waveforms Rejected by Processor 123

22. Theoretical Visibility Curves and Experimental Data 128

23. Noise on Visibility, Pedestal and A.C. Signals . . 129

NOMENCLATURE

Symbols Used throughout Text

b_0	Beam waist radius
D	Particle diameter
i	$(-1)^{1/2}$
t	Time
V	Visibility
V_0	Visibility evaluated at y = 0 or z = 0
x,y,z	Coordinates centered at beam cross-over point
x_n, y_n, z_n	Normalized coordinates x,y,z
α	Beam separation angle
δ	Fringe spacing

Symbols Used in Discussion of Optics

$E_{1,2}$	Illuminating electric fields in probe volume
E_0	Electric field magnitude at beam center line
E_s	Scattered electric field
F	Function giving dependence of scattered intensity on direction and particle parameters, for single beam illumination
I_i	Incident intensity
I_s	Scattered intensity
$\vec{K}$	Wave propagation vector
k	Wave number (= $2\pi/\lambda$)
L	Collection lens radius
P	Collected scattered light power

r_0	Radial coordinate with origin centered on collection lens
$r_{1,2}$	Radial distances on collection lens from Airy pattern centers
$\vec{r}_p$	Radial displacement of particle from center of probe volume
R	Distance from scattering particle to collection lens
x',y'	Coordinates centered on scattering particle
x_0, y_0	Coordinates centered on collection lens
Z'	Wave impedance
β	Variable in argument of Airy pattern Bessel function (= $\pi D/\delta R\alpha$)
ρ	Beam stop radius
λ	Optical wavelength
$\phi_{1,2}$	Arbitrary phase factors
ψ	Angular coordinate for circular coordinates centered on collection lens
ω_0	Optical radian frequency
ω_b	Bragg cell radian frequency
ω_s	A.C. radian frequency of optical signal

Symbols Used in Time and Frequency Domain Representations of Signals

a,b,c	Variables defined in time/frequency analysis of Chapter IV
f	Frequency
f_b	Bragg cell frequency

f_s	A.C. frequency of optical signal
$f_{10\%}$	Pedestal bandwidth
$f_{V10\%}$	Visibility bandwidth
K	Constant of proportionality
$v_{x,y}$	Components of particle velocity in x and y directions
v_p	Particle velocity
i(t)	Current as a function of time
I(f)	Fourier transform of current
V(t)	Visibility as a function of time
V(f)	Fourier transform of visibility
ω_s	A.C. radian frequency of optical signal

Symbols Used in Discussion of Circuits

A_{01}	Op-amp open loop gain
i_s	Current delivered by constant current source
R	Resistance
v	(When subscripted) voltage
V	(When subscripted) voltage

Symbols Used in Discussion of Noise

A	Processor channel gain
B_N	Noise equivalent bandwidth
f_c	Center frequency of band pass filter
G	Current gain of photomultiplier tube
$G_{vt}(f)$	Thermal noise voltage power spectral density
$G_{is}(f)$	Shot noise current power spectral density
I_p	Photodetector signal current prior to multiplier gain

$\overline{i_{ns}^2}$	Mean-square shot noise current
k	Boltzmann's constant
K	Constant of proportionality, equal to a.c. magnitude
$n(t)$	Noise voltage
$n_f(t)$	Multiplicative noise voltage
$n_c(t)$	That noise voltage which multiplies the cosine in the quadrature-carrier representation of narrowband noise
$n_s(t)$	That noise voltage which multiplies the sine in the quadrature-carrier representation of narrowband noise
q	Electronic charge
R_L	Load resistance
$r(t)$	Magnitude of narrowband signal-plus-noise voltage
$s(t)$	Signal voltage
T	Kelvin temperature
$\overline{v_{nt}^2}$	Mean-square thermal noise voltage
$\overline{v_{ns}^2}$	Mean-square shot noise voltage
$\overline{v_{1K}^2}$	Mean-square thermal noise voltage of 1K ohm resistor
σ	Standard deviation
$\phi(t)$	Phase of narrowband signal-plus-noise voltage
ω_c	Center radian frequency of band pass filter

CHAPTER I

INTRODUCTION AND BACKGROUND

I. INTRODUCTION

The recent development of laser interferometers used as velocimeters (1 through 8)[1] has made possible the accurate measurement of fluid velocity without disturbing the flow. The operation of these velocimeters may be described in terms of the Doppler shift in the frequency of light scattered from small particles in the flow, or alternatively, may be described in terms of the rate at which the particles cross real or virtual interference fringes. Determination of the sizes of the particles simultaneously with measurement of their velocity would be highly desirable, not only because size information is important in itself, but also because larger particles may not be able to exactly follow turbulent flow, resulting in inaccurate flow analysis. It has been shown that size information is in fact inherent in the scattered light signal of a laser interferometer (9, 10) and, therefore, that size and velocity may be determined simultaneously without modifying the present optical systems of velocimeters. As will be pointed out, the interferometric

---

[1]Numbers in parentheses refer to similarly numbered references in the bibliography.

method offers advantages in size determination of small particles in flows entirely apart from velocimetry.

The need exists, however, for an electronic instrument which will extract the size information from the scattered light signal. This research was undertaken to examine the theory of interferometric particle sizing in the light of electronic capabilities, in order to determine the best method for electronically extracting the size information, and to design and build an electronic processor for rapid, on-line read-out of size data.

II. LIGHT SCATTERING METHODS OF PARTICLE SIZING

Characterizing the size of small particles is important in many areas of research. A few examples are the study of atmospheric pollutants, cloud physics, rocket exhausts and fuel injection in engines, as well as wind tunnel velocimetry. In the following paragraphs, light scattering methods of size measurement are briefly reviewed. The interferometric method will be contrasted with other methods.

When an isolated particle is illuminated by a distant, monochromatic light source, the intensity I_s of the scattered light at a large distance R from the particle is given by (11):

$$I_s = \frac{I_i}{k^2R^2} F \qquad (1\text{-}1)$$

where I_i is the incident intensity, k is the wave number defined by $k = 2\pi/\lambda$ and F is a dimensionless function of the scattering direction but not of R. The function F depends in general on the shape, size and composition of the particle. The relative values of I_s (i.e., of F) may be plotted as a function of the scattering direction on a scattering diagram.

The sensitive dependence of F on particle parameters has led to a variety of light scattering experiments to determine information about the scattering particles such as their size and refractive index. Van de Hulst (11) and Kerker (12) are standard texts which discuss in detail such experiments.

Phillips and Wyatt (13), for example, used electrostatic fields to suspend atmospheric particulates in a laser beam. A photodetector was rotated around the suspended particle to map the variation in scattered intensity as a function of angle. The data obtained was used to determine optical parameters such as shape, size and refractive index. The objective of their research was to identify aerosols originating from petroleum emissions and distinguish them from similar aerosols due to other sources.

Blau, McCleese and Watson (14) report scattering experiments which used the Mie theory of scattering from homogeneous spheres of arbitrary size and composition. Hodkinson and Greenfield (15) give a theoretical discussion

of particle sizing by light scattering for a number of different optical system configurations.

Blau, et al. (16) designed an instrument to be carried in an airplane to size and count individual cloud droplets. The instrument made measurements of the light scattered from water droplets at a single angle (55 degrees) from the direction of the illuminating beam. Illumination was provided by a gallium arsenide laser diode. The theoretical scattered power as a function of droplet size was calculated using Mie theory. The theory predicts that the curve of scattered power versus size plotted on logarithmic scales will oscillate in a complicated manner for sizes near the wavelength of the illuminating light, but will be approximately linear for particles much larger or much smaller than a wavelength. For large particles, the scattered power becomes approximately proportional to the particle cross-sectional area. It is then possible to calibrate the instrument for large particles by recording the instrument response to water droplets of known size and then assuming linear variation of the log of the scattered power with the log of the droplet diameter. Droplet diameters were measured in the approximate range of 20 to 70 micrometers.

Moroz, Withstandley and Anderson (17) designed a portable instrument to size and count dust particles in mines. This instrument also made off-axis measurements of the scattered light at a single angle, 45 degrees from the

direction of the illuminating beam which in this case was a white source, a filament lamp.

Watanabe (18) recently reported the design of an instrument for sizing atmospheric pollutants in the size range 5 to 300 micrometers. The instrument was designed for on-axis measurement of the intense forward scattering lobe which is characteristic of particles much larger than the wavelength. The advantage of this arrangement is that forward scattered light is relatively independent of particle composition. An optical filter blocked the on-axis light from the laser source, preventing it from entering the photodetector. For particles greater than an order of magnitude larger than the wavelength, Fraunhofer diffraction may be applied to calculate the light scattered in the forward lobe, and this was used to determine the theoretical response of the instrument. The log of the scattered power was assumed to vary linearly with the log of the particle diameter and liquid droplets were used to calibrate the system.

Cornillault (19) described a system, also based on scalar diffraction theory, used to determine size distribution of a polydispersive sample.

Livesey and Billmeyer (20) discuss sizing using light scattered at very low angles within the forward lobe, allowing evaluation of sizes in the range 0.2 to 100 micrometers. Hodkinson (21) discusses how particles may be sized by measurements at a pair of angles within the

forward lobe. The ratio of the two intensities may be related to size.

Knollenberg (22) and Bentley (23) describe a rather direct approach to sizing, where measurement is made of the shadow area cast by a particle on a linear array composed of the exposed ends of a fiber optics bundle. Each channel in the bundle links with a photodetector which determines whether the shadow included that channel.

Holography can be used for simultaneous velocimetry and sizing (24, 25). Advantages are that the particles may be of any shape and composition and this method of sizing is quite accurate; Stigliani (26) reports an accuracy of 4 percent. Disadvantages are that two-step processing, recording and reconstruction, is required and the method is time consuming.

Those methods of sizing based on measurement of the absolute intensity of the scattered light are subject to a number of problems. As pointed out earlier, the function F of Equation 1-1 depends on the particle shape and composition as well as the size. The response of instrumentation to measure absolute intensity depends also on such variables as laser output power, photodetector sensitivity, and uniformity of sampling volume illumination.

The interferometric method of sizing described by Farmer (9, 10), being independent of the absolute value of the scattered intensity, avoids many of these difficulties. While the method is dependent on particle shape, it requires

only measurement of the relative amount of oscillation in the optical signal scattered from a particle crossing a set of fine interference fringes. The fringes are generated by an optical system identical to that of a dual-scatter laser velocimeter, and hence the method is especially convenient for use in conjunction with velocimetry.

The theory of interferometric particle sizing will be discussed in detail in Chapter II. The visibility of the scattered light waveform of a passing particle will be defined and its relation to the size of the scattering particle will be derived using scalar diffraction theory. The manner in which the waveform varies as a particle passes through the probe volume will be examined in Chapter III in order to determine means for electronically measuring the visibility. The frequency spectrum of the scattered light signal will be derived in Chapter IV. The details of a circuit constructed to process the interferometer signal and measure the visibility will be presented in Chapter V. Circuit performance and noise analysis are the subjects of Chapters VI and VII, respectively. Results of particle size measurement using the signal processor will be reported in Chapter VIII, and in Chapter IX will be presented conclusions and recommendations for future research.

CHAPTER II

INTERFEROMETRIC PARTICLE SIZE ANALYSIS: RELATION OF VISIBILITY TO PARTICLE SIZE

Laser interferometers are being used to measure the velocity of small particles. As discussed in Chapter I, they may also be used to measure particle size. This chapter will review interferometric particle sizing, beginning with a description of the intensity distribution in the region where two laser beams are simultaneously crossed and focused.

I. INTENSITY DISTRIBUTION IN THE PROBE VOLUME

An optical arrangement for generating a set of high contrast fringes is shown in Figure 1. The laser beam (assumed to be in the TEM_{00} mode) is split into two beams which are then caused by a lens to both cross and focus at a common point. The two beams are of equal intensity and linearly polarized in the same direction. At the cross point, each beam focuses to a waist containing planar wavefronts. A coordinate system is defined as shown in Figure 1 such that z lies along the bisector of the beams, x is in their direction of polarization, y is orthogonal to x and z, and the origin is at the cross-point of the beams.

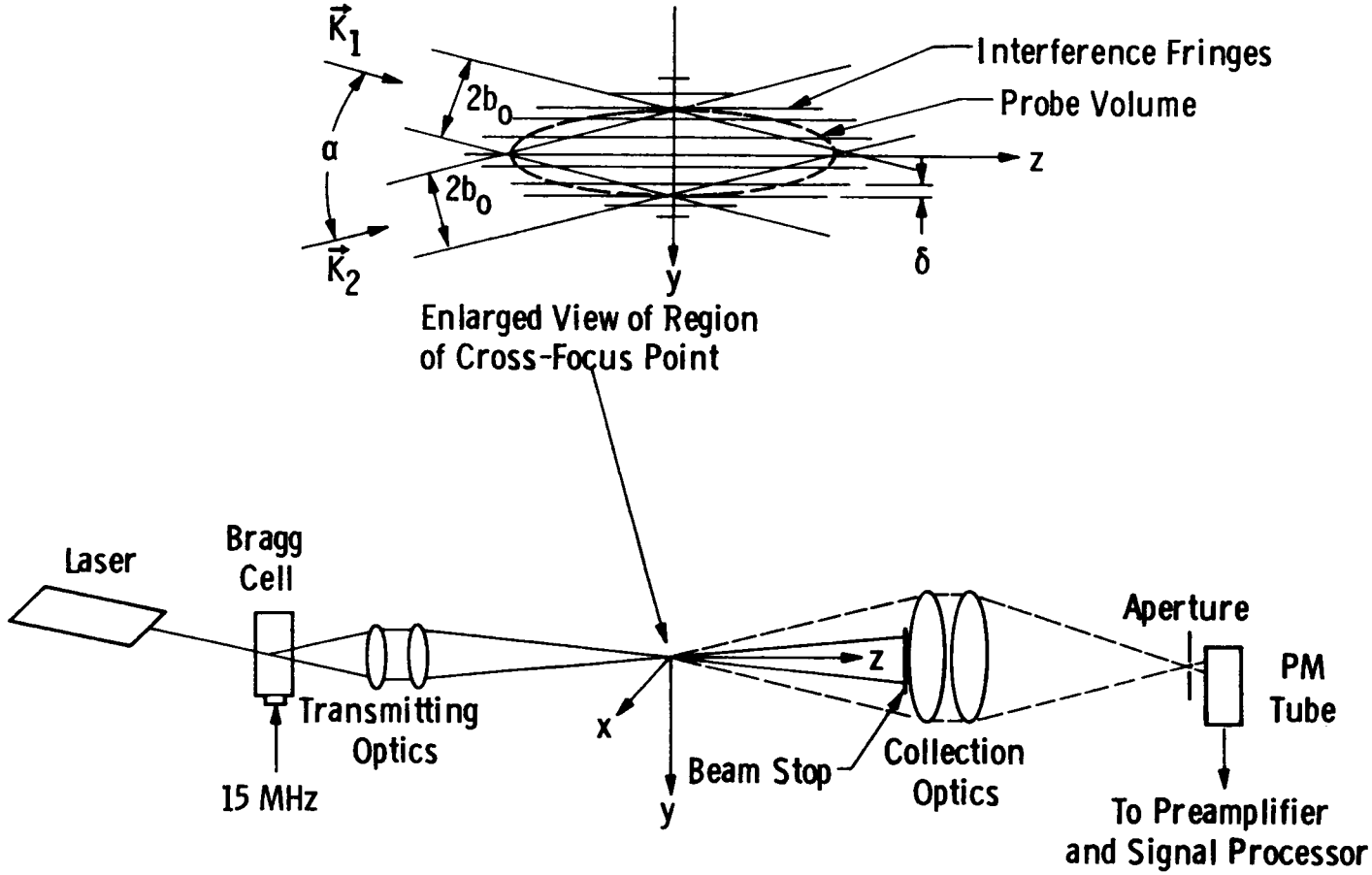


Figure 1. Optical arrangement for generating a set of interference fringes.

The splitting of the beams is accomplished either by beam-splitting glass blocks, which produce stationary fringes in the region where the beams cross, or by a Bragg cell (27, 28), which produces moving fringes. In the Bragg cell, ultrasonic sound waves in water diffract one beam and increase its frequency by an amount equal to the frequency of the sound waves.

Assuming a Bragg cell is used, let the electric fields E_1 and E_2 of the two laser beams in the region of cross-over be expressed as (1)

$$E_1 = E_0 \exp[-(x_1^2 + y_1^2)/b_0^2] \exp[-i\omega_0 t + i\vec{K}_1 \cdot \vec{r}_p + i\phi_1]$$

$$E_2 = E_0 \exp[-(x_2^2 + y_2^2)/b_0^2] \exp[-i(\omega_0 + \omega_b)t + i\vec{K}_2 \cdot \vec{r}_p + i\phi_2] \qquad (2\text{-}1)$$

where E_0 is the field magnitude on the center line of each beam, b_0 is the beam waist radius (further discussed below), ω_0 is the optical radian frequency, ω_b is the Bragg cell radian frequency, $|\vec{K}_1| = 2\pi/\lambda \simeq |\vec{K}_2|$ (where λ is the laser optical wavelength), $\vec{r}_p$ is a vector from the origin to the point x, y, z, and ϕ_1, ϕ_2 are arbitrary phase factors.

Each electric field is expressed in terms of its own coordinate system (see Figure 2) referred to its own direction of propagation: z_i is in the direction of propagation of the "ith" beam, x_i is in the direction of polarization and y_i is orthogonal to the x_i z_i plane. The origin of both these coordinate systems is also located at the

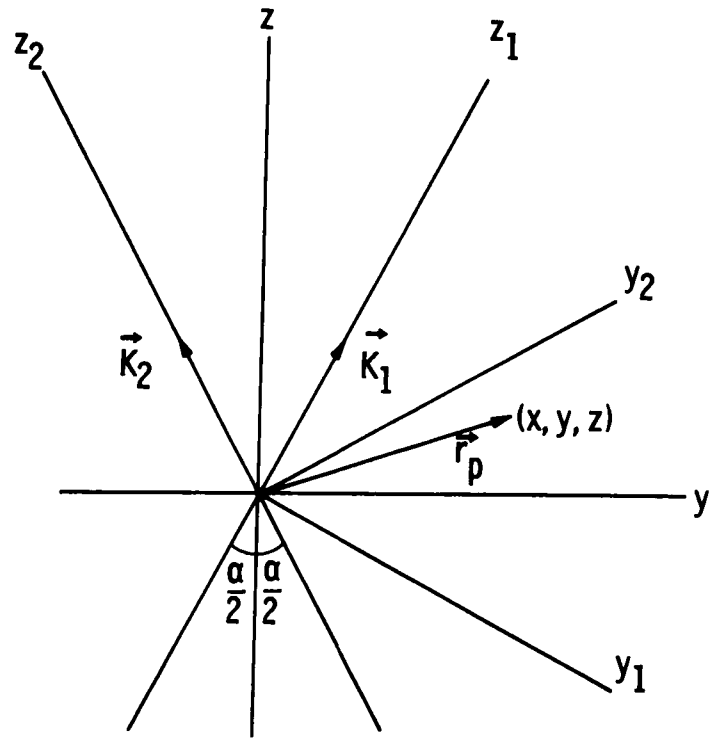


Figure 2. Geometry for two crossed laser beams, $\vec{K}_1$ and $\vec{K}_2$.

cross-focus point of the two beams, as is the coordinate system introduced in Figure 1, page 9. Since the beams are polarized in the same direction, $x_1 = x_2 = x$ and ϕ_1 will arbitrarily be set equal to ϕ_2 (which simply places a bright fringe at the origin when $t = 0$).

The waist radius b_0 is the radial distance from center line of each beam to where the field amplitude of that beam has fallen off to e^{-i} times its value on center line. The amplitude falls off in a Gaussian manner with radial distance equal to $(x^2 + y_i^2)^{1/2}$, as given by the exponential factor containing b_0 in each equation.

The two plane wave radiations interfere to form a fringe system. By summing E_1 and E_2 of Equations 2-1 and transforming coordinates to the symmetrically located coordinates xyz, the intensity I_i in the cross-over region can be expressed as

$$I_i = (E_1 + E_2)(E_1^* + E_2^*)/2Z'$$

$$= \frac{E_0^2}{Z'} \exp\left[-\frac{2}{b_0^2}\left(x^2 + y^2 \cos^2\frac{\alpha}{2} + z^2 \sin^2\frac{\alpha}{2}\right)\right]$$

$$\times \left[\cosh\left(\frac{2}{b_0^2} yz \sin\alpha\right) + \cos[\omega_b t + (\vec{K}_1 - \vec{K}_2) \cdot \vec{r}_p]\right]$$

where Z' is the wave impedance of the surrounding medium and α is the angle of separation between the beams. Further observing from Figure 2 that

$$(\vec{K}_1 - \vec{K}_2) \cdot \vec{r}_p = 2|\vec{K}_1| \, y \sin(\alpha/2)$$

we may write

$$I_i = \frac{E_0^2}{Z^1} \exp\left[- \frac{2}{b_0^2}\left(x^2 + y^2 \cos^2 \frac{\alpha}{2} + z^2 \sin^2 \frac{\alpha}{2}\right)\right] \times \left[\cosh\left(\frac{2}{b_0^2} yz \sin \alpha\right) + \cos(\omega_b t + 2\pi y/\delta)\right] \qquad (2\text{-}2)$$

where $\delta = \lambda/(2 \sin(\alpha/2))$ is the fringe spacing.

Equation 2-2 shows that the only dependence of the fringe pattern on x is in the factor $\exp(-2x^2/b_0^2)$; the intensity distribution does not vary in the x direction except to decrease in a Gaussian manner. Reference (1) includes a sketch of Equation 2-2 for the plane x = 0 at time t = 0, which is reproduced here as Figure 3. The fringes are planes extending parallel to the xz plane and move in the negative y direction. For z = 0 the cosh term is unity for all y, and the distribution consists of alternate bright and dark fringes decreasing in intensity in a Gaussian manner in the y direction. Farther out on the z-axis, beyond the cross-over point of the beams, the cosh term becomes significant and the mean intensity of the illumination increases somewhat in the y direction before the Gaussian fall-off causes the intensity to go to zero. One can visualize in Figure 3 the beams separating beyond the cross-over point.

The "probe volume" is defined (2) from Equation 2-2 as that volume within the surface where the Gaussian factor

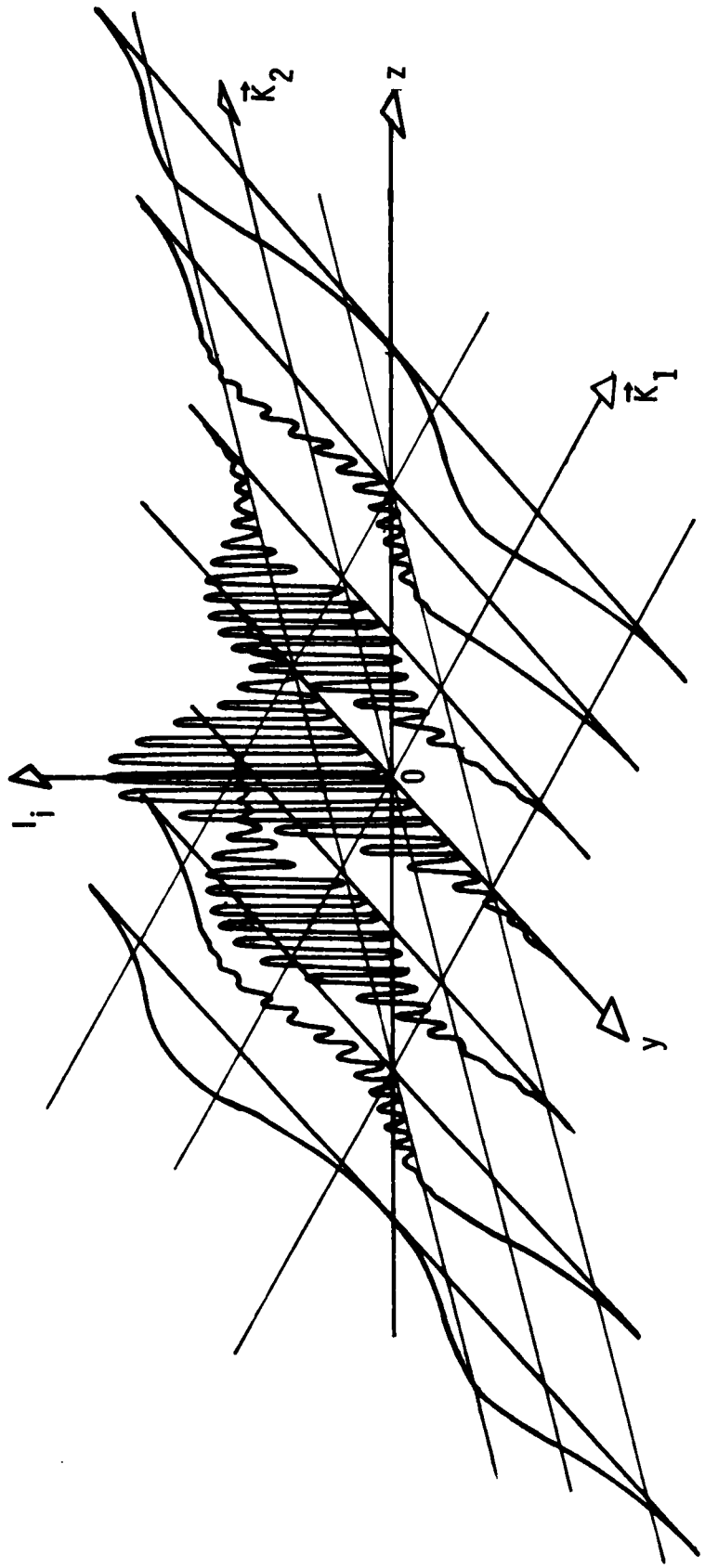


Figure 3. Intensity distribution in the probe volume.

$$\exp\left[-\frac{2}{b_0^2}\left(x^2 + y^2\cos^2\frac{\alpha}{2} + z^2\sin^2\frac{\alpha}{2}\right)\right]$$

has decreased to e^{-2}. Setting $y = z = 0$, the point where this ellipsoidal surface intersects the x-axis is found to be

$$\exp\left[-\frac{2}{b_0^2}x^2\right] = e^{-2}$$

$$x = b_0 \qquad (2\text{-}3a)$$

Similarly, the y- and z-axis intersections are

$$y = b_0/\cos(\alpha/2) \qquad (2\text{-}3b)$$

$$z = b_0/\sin(\alpha/2) \qquad (2\text{-}3c)$$

Note that for a beam separation angle α that is typically small, the probe volume ellipsoid is cigar shaped, extending considerably farther in the z direction than in either the x or y directions. In practice, the probe volume may extend only a few tens of micrometers in the x and y directions.

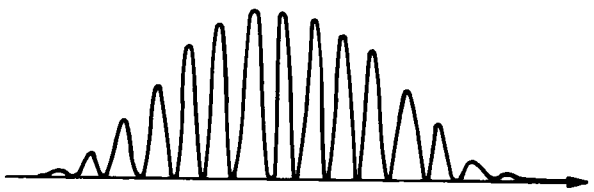
Collection lenses shown in Figure 1, page 9, collect the light and a photomultiplier tube (PM tube) detects the light signal scattered from a particle which passes through the fringe system.

II. RELATION OF VISIBILITY TO PARTICLE SIZE: FRINGE MODEL

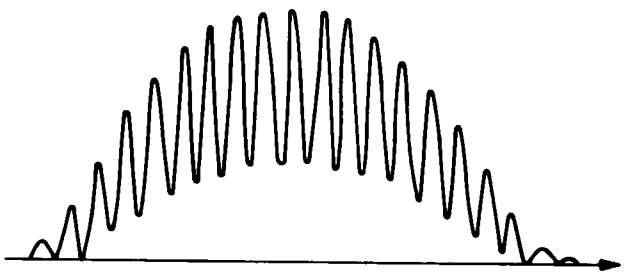
Suppose a particle whose dimensions are very small compared to the fringe spacing passes through the probe volume. The detected optical signal will trace out the illuminating intensity I_i in the probe volume. For example, if a small particle moves along the y-axis, the signal as viewed on an oscilloscope connected to the PM tube will trace out the waveform depicted in Figure 4a. Here the signal alternately builds up as the scatterer crosses a bright fringe, then falls to zero as the scatterer passes through a dark fringe. The peak signal crossing the bright fringes increases as the particle approaches the center of the fringe set, then decreases as the particle leaves.

(Laser velocimeters determine the component of particle velocity orthogonal to the fringe planes by measuring the time period of the oscillating light signal. The fringe spacing divided by the time required for the particle to move from one fringe to the next is equal to its velocity. If moving fringes are used, their velocity must also be taken into account.)

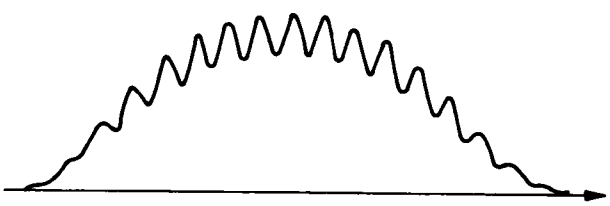
Now suppose the particle is not very small compared to a fringe spacing. It cannot be completely hidden in a dark fringe because its size will partially overlap the two adjoining bright fringes. A larger particle following the same path as the small particle just discussed might produce



a. Visibility = 1.0



b. Visibility = 0.47



c. Visibility = 0.17

Figure 4. Scattered intensity for three values of D/δ, $z = 0$.

the signal shown in Figure 4b. Here the scattered waveform does not fall all the way to zero between bright fringes because the particle is always intercepting some light. A still larger particle, overlapping yet more of the adjoining fringes during its traversal, might produce a signal similar to that of Figure 4c. It can be seen that the magnitude of oscillation (relative to the signal as a whole) decreases with increases in particle size, at least initially. In fact, for certain particle dimensions it might be wondered if the PM tube signal would display only a Gaussian form with no oscillation on it, and in fact theory to be developed will show this result. Durst (7, page 642) gives a qualitative description of this effect.

A solution for the waveform of the detected scattered light must take into account the fact that light from each illuminating beam is scattered in lobes independently of that from the other beam. The scattered fields from both beams must be summed at any observation point to find the scattered intensity there. The case of the light scattered from a single particle illuminated by two beams has been considered (9, 10), using equations for the fields scattered from a spherical particle immersed in a dielectric medium scattering plane waves (12). It was shown that when the two illuminating beams are polarized in the same direction and have equal intensities, the scattered intensity observed on the axis between the beams is proportional to the illuminating intensity at the particle's location.

To account for the nonuniform illumination of the particle by the interfering light beams, and to relate the scattered intensity to size, the assumption was made (9, 10) that the scattered intensity collected paraxially is proportional to the mean illuminating intensity over the particle's two-dimensional geometrical cross-section; that is, that the scattered intensity I_s can be written as

$$I_s \sim \frac{1}{A_p} \iint_{A_p} I_i \, dx \, dy \qquad (2\text{-}4)$$

where A_p is the cross-sectional particle area and the incident intensity I_i is given by Equation 2-2. Thus this "fringe model" approach indicates that the observed intensity can be found by averaging the illuminating fringe intensity over the particle's cross-section.

The integration of I_i indicated by Equation 2-4 over an arbitrary cross-sectional area is not easily obtained. However, if a simplifying assumption is made, closed form solutions can be found for the cross-sectional areas of certain shapes, including spheres and cylinders. The assumption is made that the maximum particle dimension D is small compared to the beam radius b_0. This makes it possible to assume that the slowly varying exponential and cosh terms of Equation 2-2 remain constant over the scatterer surface.

With the assumption that $b_0 >> D$, and using Equation 2-2, Equation 2-4 may be written

$$I_s \sim \exp\left[-\frac{2}{b_0^2}\left(x^2 + y^2 \cos^2\frac{\alpha}{2} + z^2 \sin^2\frac{\alpha}{2}\right)\right] \times \left[\cosh\left(\frac{2}{b_0^2} yz \sin\alpha\right) + \frac{1}{A_p}\iint_{A_p} \cos[\omega_b t + 2\pi(y + y')/\delta] \times dx'dy'\right]$$

where x, y and z now represent the coordinates of the center of the particle and x' y' are coordinates on the particle cross-sectional area with origin at the particle center.

Straightforward transformation to circular coordinates and then carrying out the integration for the cross-sectional area of a sphere gives

$$I_s \sim \exp\left[-\frac{2}{b_0^2}\left(x^2 + y^2 \cos^2\frac{\alpha}{2} + z^2 \sin^2\frac{\alpha}{2}\right)\right] \times \left[\cosh\left(\frac{2}{b_0^2} yz \sin\alpha\right) + V_0 \cos(\omega_b t + 2\pi y/\delta)\right] \qquad (2\text{-}5)$$

where

$$V_0 = \frac{2J_1(\pi D/\delta)}{(\pi D/\delta)}$$

and $J_1(\ )$ is a first order Bessel function of the first kind.

Equation 2-5 is an expression for the light scattered from a spherical particle of diameter D located at point x,y,z, where the dependence of the signal shape on the diameter is given by V_0. If a particle follows some trajectory through the fringe set near z = 0 and the signal is displayed on an oscilloscope screen, the result might look like any of the waveforms of Figure 4, page 17, depending on the ratio of the diameter and the fringe spacing.

Equation 2-5 represents the sum of a Gaussian-modulated cosh function, known as the "pedestal," and a Gaussian-modulated cosine, known as the "a.c." component of the signal. The ratio of the a.c. magnitude to the pedestal at a point (x,y,z) is defined as the "visibility," V:

$$V \triangleq \frac{\text{a.c. magnitude}}{\text{pedestal}} \tag{2-6}$$

From Equation 2-5, this is given by

$$V = \frac{V_0}{\cosh\left(\frac{2}{b_0^2}\, yz \sin\alpha\right)} \tag{2-7}$$

It can be seen that in either the xy plane (z = 0) or the xz plane (y = 0), the cosh term of Equation 2-7 is equal to one, and the visibility reduces to the numerator of Equation 2-7. In either of these planes, the visibility is given by V_0 and is a function only of D/δ; i.e., for a sphere,

$$V = V_0 = \frac{2J_1(\pi D/\delta)}{(\pi D/\delta)} \quad (y = 0 \text{ or } z = 0) \tag{2-8}$$

Equation 2-8 for the visibility V_0 as a function of D/δ is plotted in Figure 5 as the curve labeled "Fringe Model." Examination of the curve shows that the visibility has zeros; i.e., for certain particle dimensions, no a.c. term will appear. It can also be seen that for visibilities less than about 0.15, different particle sizes can have the same visibility. It should also be noted that the visibility changes sign as it passes through successive zeros. (This is not shown in Figure 5, which plots only the absolute value of the visibility.) Negative visibility means that more light is scattered when the particle is centered over a dark fringe and overlapping adjoining bright fringes than when it is centered over a bright fringe.

III. RELATION OF VISIBILITY TO PARTICLE SIZE: SCALAR DIFFRACTION THEORY

Data obtained in the course of this work and reported in Chapter VIII do not agree with the fringe model prediction. Scalar diffraction theory was then studied for application to this problem. In the region in which it can be applied, Fraunhofer diffraction can be used to proceed directly to a solution for the relation of visibility to size. The procedure is to first find the diffracted field in the plane of the collection lens due to each of the incident beams, then to sum these fields and find the

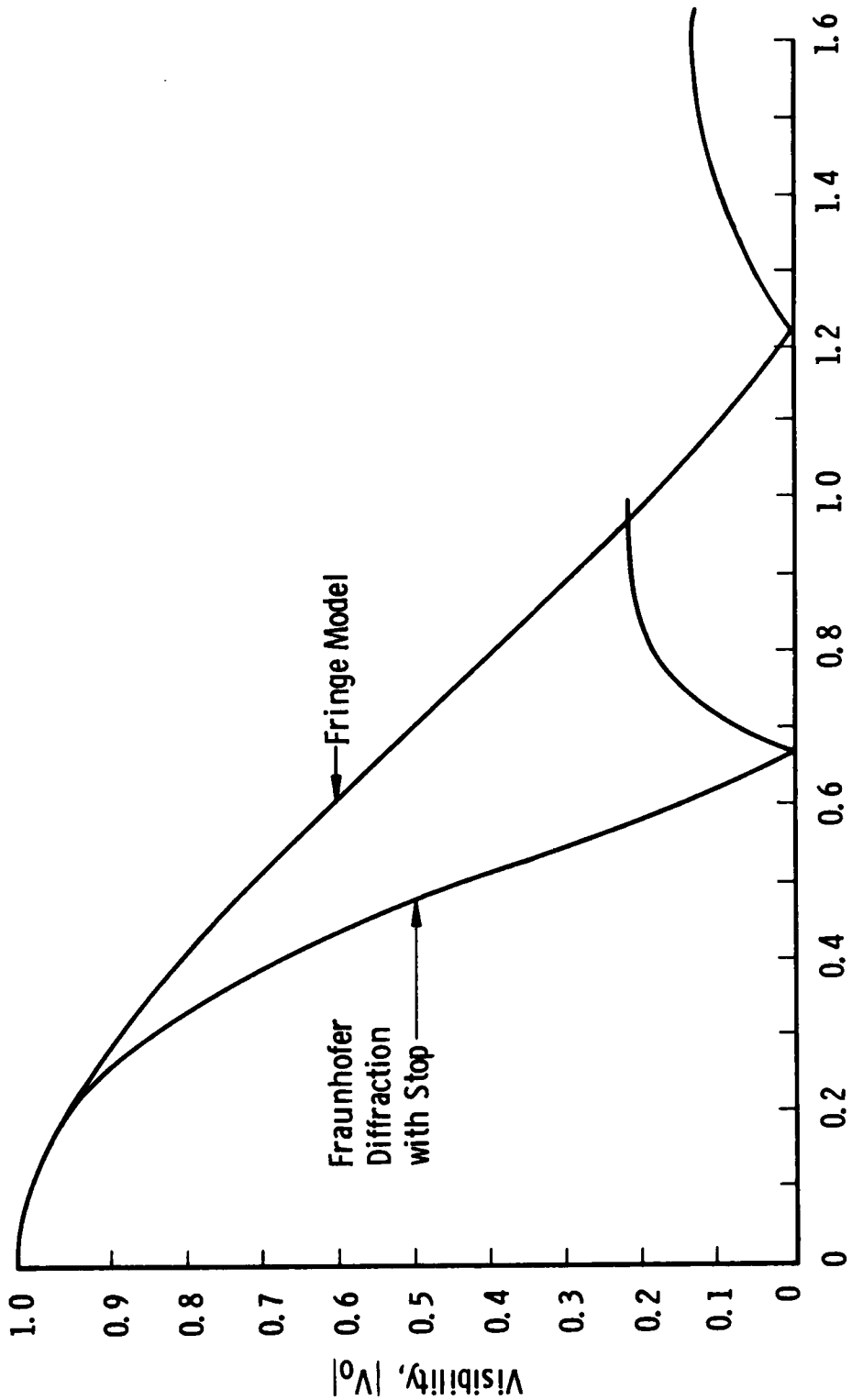


Figure 5. Theoretical curves of visibility V_0 versus ratio of diameter to fringe spacing D/δ.

resultant intensity. This intensity distribution is then integrated over the area representing the collection lens in order to find the total power collected and transmitted to the photodetector. Assumptions made are the usual ones made in order to apply Fraunhofer diffraction (29); i.e., the sphere diameter D is assumed large compared with the illuminating wavelength λ and the diffracted light is observed near the optical axis of each beam (requiring that the beam separation angle α be small) and at a distance $R >> D^2/\lambda$. The assumption will also again be made that the sphere diameter is much less than the beam waist radius b_0.

Each diffracted field is found by integrating the illuminating field over an aperture located in the object plane (in the crossover region of the illuminating beams). Babinet's principle (30) shows that the diffracted intensity distribution calculated will be the same when the aperture is replaced by an opaque disc (as an approximation of the sphere).

The electric fields of the two beams incident on the particle are given by Equation 2-1, page 10. From the geometry of Figure 2, page 11, it may also be seen that

$$\vec{K}_1 \cdot \vec{r}_p = ky \sin(\alpha/2) + kz \cos(\alpha/2)$$

$$\vec{K}_2 \cdot \vec{r}_p = -ky \sin(\alpha/2) + kz \cos(\alpha/2)$$

where $|\vec{K}_1|$ and $|\vec{K}_2|$, which are approximately equal, have been replaced by $k = 2\pi/\lambda$. Since the fringe spacing δ is

given by $\delta = \lambda/(2 \sin(\alpha/2))$, these relations may be written

$$\vec{K}_1 \cdot \vec{r}_p = (\pi y/\delta) + kz \cos(\alpha/2)$$

$$\vec{K}_2 \cdot \vec{r}_p = (-\pi y/\delta) + kz \cos(\alpha/2)$$

Transforming the y_1 and y_2 coordinates to the symmetrically located coordinates xyz by the transformation relations

$$y_1 = y \cos(\alpha/2) - z \sin(\alpha/2)$$

$$y_2 = y \cos(\alpha/2) + z \sin(\alpha/2)$$

and letting $\phi_1 = \phi_2$ and $x_1 = x_2 = x$ as before, and also letting $\sin \alpha \simeq \alpha$, $\cos \alpha \simeq 1$ since α is small, the Equations 2-1 may be rewritten

$$E_1 = A(x,y,z) \exp[-i\omega_0 t + i(kz + \pi y/\delta)]$$

$$E_2 = B(x,y,z) \exp[-i(\omega_0 + \omega_b)t + i(kz - \pi y/\delta)]$$

where

$$A(x,y,z) = E_0 \exp[-(x^2 + y^2 - yz\alpha + z^2\alpha^2/4)/b_0^2]$$

and

$$B(x,y,z) = E_0 \exp[-(x^2 + y^2 + yz\alpha + z^2\alpha^2/4)/b_0^2]$$

In the integration over the aperture to find the diffracted fields, the amplitude terms A and B of these equations will be considered constants (since these terms

are slowly varying under the assumption that the sphere is much smaller than the beam radius). In the phase terms of these equations, the coordinate y will be replaced by $(y + y')$, letting the coordinates x,y,z become the (constant) coordinates of the aperture center. Integration will be with respect to x' and y', coordinates with origin at the aperture center. The equations become

$$E_1 = A(x,y,z)\ \exp\{-i\omega_0 t + i[kz + \pi(y + y')/\delta]\}$$

$$E_2 = B(x,y,z)\ \exp\{-i(\omega_0 + \omega_b)t + i[kz - \pi(y + y')/\delta]\} \quad (2\text{-}9)$$

The diffracted field due to each of these illuminating fields is found by an integration over the aperture which is equivalent to finding the two-dimensional Fourier transform of the illuminating field, evaluated at frequencies $f_x = x_0/\lambda R$ and $f_y = y_0/\lambda R$, where R is the distance from the aperture to the plane of the collection lens and x_0, y_0 are coordinates centered on the collection lens.

Examination of Equations 2-9 shows that they consist of factors that will be constant in the integration with respect to x', y', multiplied by a phase factor. The first equation has the phase factor $\exp(i\pi y'/\delta)$ and the second has the phase factor $\exp(-i\pi y'/\delta)$.

The shift theorem of Fourier transform theory states that

$$\mathcal{F}\{g(x',y')\ \exp(i2\pi f y')\} = G(f_x, f_y - f)$$

where

$$\mathcal{F}\{g(x',y')\} = G(f_x,f_y)$$

That is, the transform of a function in the object plane which is multiplied by a phase term is simply spatially shifted in the observation plane.

The problem for each beam reduces, then, to finding the Fourier transform of a uniform field illuminating a circular aperture, then shifting the diffracted field in the observation plane. This problem has already been worked out (e.g., Reference (29)); the desired diffracted fields are simply spatially shifted Airy patterns and may be written down as follows:

$$E_{s1} = -iA(x,y,z)(kD^2/8R)\ \exp[ikR + ikr_0^2/2R]$$
$$\times \exp[-i\omega_0 t + i(kz + \pi y/\delta)]\left(\frac{2J_1(\beta r_1)}{\beta r_1}\right)$$

$$E_{s2} = -iB(x,y,z)(kD^2/8R)\ \exp[ikR + ikr_0^2/2R]$$
$$\times \exp[-i(\omega_0 + \omega_b)t + i(kz - \pi y/\delta)]\left(\frac{2J_1(\beta r_2)}{\beta r_2}\right) \qquad (2\text{-}10)$$

where $A(x,y,z)$ and $B(x,y,z)$ are the functions previously defined, and where

$$r_0^2 = x_0^2 + y_0^2$$

$$r_1^2 = x_0^2 + (y_0 - \lambda R/2\delta)^2$$

$$r_2^2 = x_0^2 + (y_0 + \lambda R/2\delta)^2$$

$\beta = kD/2R = \pi D/\lambda R$

Using $\delta \simeq \lambda/\alpha$, β may be written as a function of D/δ:

$\beta = \pi D/\delta R\alpha$

The diffraction geometry is sketched in Figure 6. Equations 2-10 represent the fields diffracted from two beams (separated by a small angle α) by an aperture representing a sphere of diameter D located at coordinates (x,y,z) in the crossover region of the beams (probe volume). The fields are observed close to the optical axis at coordinates (x_0,y_0) on the collection lens located a distance R from the probe volume. The variable δ is the interference fringe spacing in the probe volume. Each diffracted field is an Airy pattern, centered on the y_0 axis at a distance $\lambda R/2\delta$ from the collection lens center; the variables r_1 and r_2 are radial distances from the center of each Airy pattern.

The intensity I_s at any point x_0,y_0 on the collection lens is given by

$$I_s=(E_{s1} + E_{s2})(E^*_{s1} + E^*_{s2})/2Z'$$

where Z' is the wave impedance of the surrounding medium. Substituting the equations for E_{s1} and E_{s2} into this expression and carrying out the indicated multiplication gives

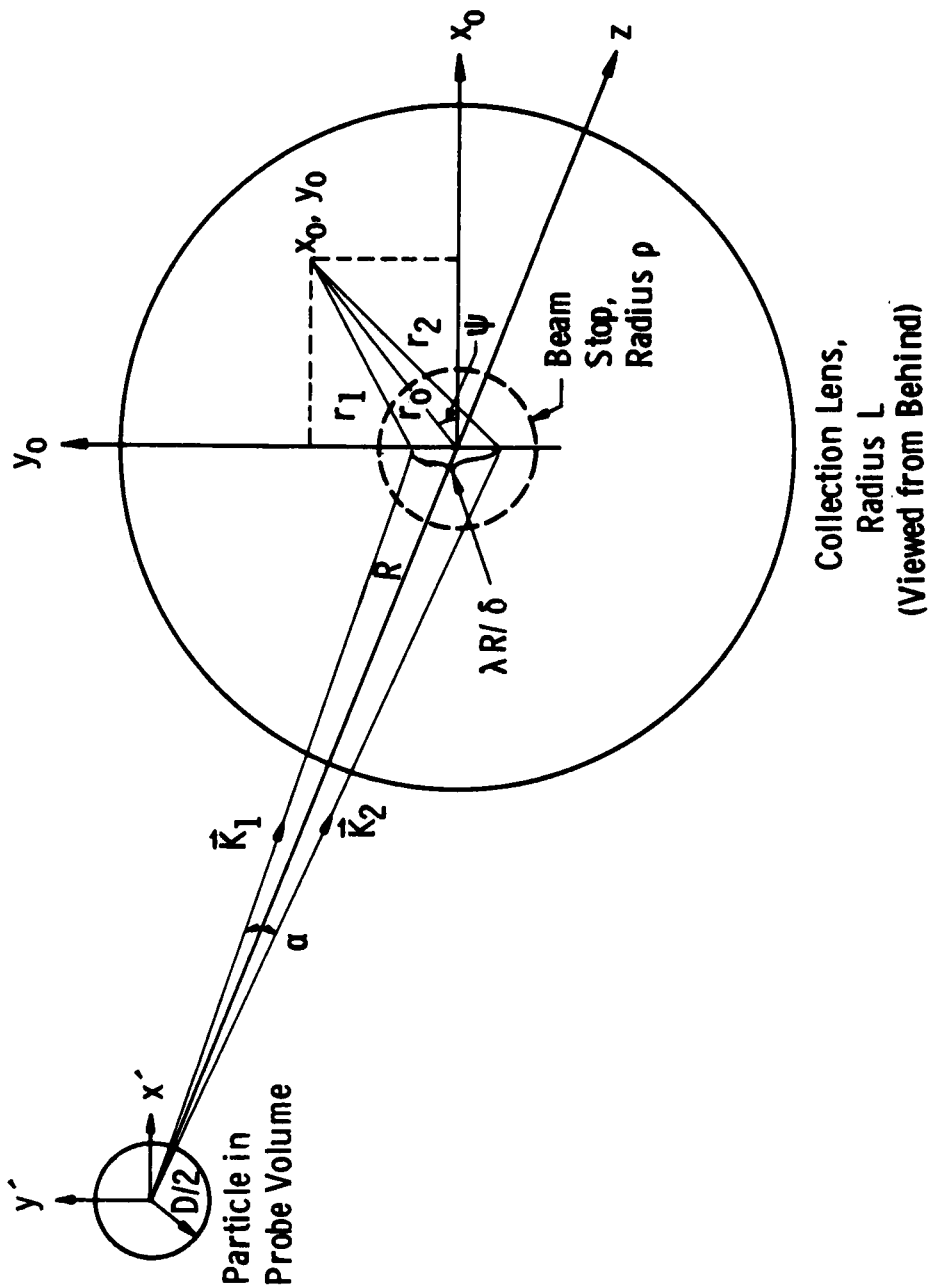


Figure 6. Diffraction geometry.

$$I_s = \frac{E_0^2 k^2 D^4}{32 Z'^2 R^2} \exp\left[-\frac{2}{b_0^2}(x^2 + y^2 + z^2\alpha^2/4)\right]$$

$$\times \left[\frac{J_1^2(\beta r_1)}{(\beta r_1)^2} \exp(2yz\alpha/b_0^2) + \frac{J_1^2(\beta r_2)}{(\beta r_2)^2} \exp(-2yz\alpha/b_0^2)\right.$$

$$\left. + 2\,\frac{J_1(\beta r_1)}{(\beta r_1)}\,\frac{J_1(\beta r_2)}{(\beta r_2)} \cos(\omega_b t + 2\pi y/\delta)\right] \qquad (2\text{-}11)$$

This expression for the diffracted intensity must be integrated over the collection lens to find the total power collected and transmitted to the photodetector. A simplification of the resultant expression is obtained if it is noticed that the integrals of two of the terms are equal by consideration of the symmetry of the problem; i.e.,

$$\int_0^{2\pi}\int_0^{L} \frac{J_1^2(\beta r_1)}{(\beta r_1)^2}\, r_0 dr_0 d\psi = \int_0^{2\pi}\int_0^{L} \frac{J_1^2(\beta r_2)}{(\beta r_2)^2}\, r_0 dr_0 d\psi \qquad (2\text{-}12)$$

where L is the radius of the collection lens. With this observation, the collected power may be written

$$P = \frac{E_0^2 k^2 D^4}{32 Z'^2 R^2} \exp\left[-\frac{2}{b_0^2}(x^2 + y^2 + z^2\alpha^2/4)\right]$$

$$\times \left[\cosh(2yz\alpha/b_0^2) \int_0^{2\pi}\int_0^{L} \left[\frac{J_1^2(\beta r_1)}{(\beta r_1)^2} + \frac{J_1^2(\beta r_2)}{(\beta r_2)^2}\right] r_0 dr_0 d\psi\right.$$

$$\left. + 2\cos(\omega_b t + 2\pi y/\delta) \int_0^{2\pi}\int_0^{L} \frac{J_1(\beta r_1)}{(\beta r_1)}\,\frac{J_1(\beta r_2)}{(\beta r_2)}\, r_0 dr_0 d\psi\right] \qquad (2\text{-}13)$$

(The terms (Equation 2-12) which are equal to each other are both shown simply for symmetry of notation.)

The visibility of this collected power waveform is defined as before as the ratio of the magnitude of the cosine term to the pedestal, and may be written

$$V = \frac{V_0}{\cosh\left(\frac{2}{b_0^2}\, yz\alpha\right)} \tag{2-14}$$

where

$$V_0 = \frac{2\int_0^{2\pi}\int_0^{L} \frac{J_1(\beta r_1)}{(\beta r_1)}\,\frac{J_1(\beta r_2)}{(\beta r_2)}\, r_0 dr_0 d\psi}{\int_0^{2\pi}\int_0^{L}\left[\frac{J_1^2(\beta r_1)}{(\beta r_1)^2} + \frac{J_1^2(\beta r_2)}{(\beta r_2)^2}\right] r_0 dr_0 d\psi} \tag{2-15}$$

Equation 2-14 has the same form as Equation 2-7, page 21 (with sin α set equal to α since α is here assumed small), showing that the predicted variation of the visibility with the particle's spatial coordinates is the same in both cases. The question remains whether the visibility's variation with D/δ contained in β in Equation 2-15 is the same as that predicted by the fringe model in Equation 2-8, page 22.

Equation 2-15 was evaluated on a computer using the limits of integration shown and the numerical results fell closely on the fringe model prediction of Equation 2-8, which would confirm the validity of the fringe model

for the assumed conditions.

It is not possible in practice, however, to collect the diffracted light over the entire lens, since a light stop must be used at the center of the lens to block the projected incident laser source beams. Evaluation of Equation 2-15 with the lower radial limit of integration changed from 0 to ρ, where ρ is the radius of the circular beam stop, resulted in the curve of Figure 5, page 23, labeled "Fraunhofer Diffraction with Stop." For computation of the particular curve shown, it was assumed the collection lens was an F/5, six-inch diameter lens with a 2 cm diameter light stop; α was 0.01 radian.

Data reported in Chapter VIII are better explained by the Fraunhofer diffraction curve shown than by the fringe model prediction. This will be further discussed in that chapter and in the concluding chapter.

The important conditions and assumptions discussed in this chapter for interferometric particle size measurement may be summarized as follows.

1. The two illuminating beams are of the same center-line intensity and are both polarized in the same direction.
2. The particle is spherical in shape.
3. The particle is small compared to the beam waist radius.
4. The visibility is measured when the particle is in either the $y = 0$ or the $z = 0$ plane, where it

is given by V_0, a function only of the ratio of diameter to fringe spacing for a given optical system. This may require that the particles move in a particular direction so that they will cross either the y = 0 or the z = 0 plane.

5. The scattered light is collected by a lens centered on the axis bisecting the beams (i.e., paraxially); Fraunhofer diffraction requires that the light be collected close to the optical axis of each beam, requiring that the beam separation angle α be small.
6. For Fraunhofer diffraction, it is further required that the particle diameter D be large compared to the illuminating wavelength λ and that the distance R to the collection lens be large compared to D^2/λ.
7. It has been tacitly assumed that only one particle occupies the probe volume at a time. Results obtained in this chapter are specifically for a single scattering particle and do not apply when there are multiple particles simultaneously occupying the probe volume.

It may be noted that the visibility as defined at a point on the waveform by Equation 2-6 differs slightly from the usual definition of the visibility of fringes, originally due to Michelson (30). Michelson's definition is based on the maximum intensity in a bright fringe and the minimum

intensity in an adjoining dark fringe and approximates the definition of Equation 2-6. The visibility as defined in Equation 2-6 is preferred here because it arises naturally in the expression for the scattered optical signal and contains the size dependence of the waveform. Further, it may be measured using electronic circuitry as will be described in Chapter III.

CHAPTER III

ELECTRONIC METHODS OF VISIBILITY MEASUREMENT

I. INTRODUCTION

The relation of the visibility to the size of the particle was discussed in Chapter II. It was noted that if the visibility given by Equation 2-7 is measured when the particle is in either the xy plane or the xz plane of Figure 1, page 9, then the visibility measured is V_0, a function of the particle size. Variations in the scattered light waveform as a given particle passes through the system are investigated in this chapter in order to find electronic methods of making this measurement.

The simplest method to obtain the signal visibility is to display the photodetected signal on an oscilloscope. The waveform may be photographed, and the ratio of the a.c. to the pedestal may then be measured directly from the photograph. Measuring the visibility in this manner is obviously time consuming.

Very fast transient waveform recorders are available which digitize signals having a.c. components in the hundreds of megahertz range. Such an instrument could record the waveform, digitize it and transfer it into a digital computer for analysis and extraction of the visibility. A large computer program would be required, and although very

high frequency waveforms could be captured, the measurement repetition rate would be quite low.

Analog circuitry, on the other hand, can provide a high data rate, with the capability of sizing thousands of particles per second. The visibility can be read out directly by the instrument, requiring only conversion to particle dimension. The development of analog circuitry will be the primary topic of this chapter, although many of the results can be applied also to digital methods.

II. OPTICALLY APERTURED SYSTEM: PEAK DETECTORS

In a typical laser interferometer system used for measuring particle velocity, the particles move generally in the x or y direction of Figure 1, page 9, passing in front of the beam producing optics. Because of the elongation of the probe volume in the z direction, small motion in the z direction can be disregarded. One method to ensure that the visibility is measured only for particles whose z coordinate is at (or near) zero, thus measuring V_0, is to use an optical aperture so that light is collected only from the region in (or near) the z = 0 plane. Assuming particles move with constant velocity, the waveform versus time will look like any of those in Figure 4, page 17, depending on the value of V_0.

The higher frequency a.c. term can be separated from the lower frequency pedestal by filtering. Since the

visibility throughout the z = 0 plane is a constant, equal to V_0, electronic peak detectors may be used to separately measure the peak values reached by the a.c. and the pedestal, and the visibility V_0 may be determined by dividing the two values.

Figure 7 is a block diagram showing the electronics for measuring visibility by this method. Peak detectors follow the filters to record the peak values reached. The a.c. peak is then divided by the pedestal peak in an analog divider. Because peak detectors store their values on capacitors which bleed off in time, the divider output must be converted to digital form for storage until it can be transferred to an external recording device.

The trajectory of the particle is unimportant in this method (so long as it remains close to the xy plane) except that for stationary fringes, the particle must have a sufficient component of velocity in the y direction to adequately display the cosine term. The waveform should oscillate enough times during the particle's traversal so that the cosine will oscillate to a maximum while the modulating Gaussian exponential is also at its peak, in order for the maximum cosine magnitude to be recorded by the peak detector. If the fringes are themselves rapidly moving by the particle to display the cosine, the direction of the particle's trajectory through the xy plane is entirely immaterial.

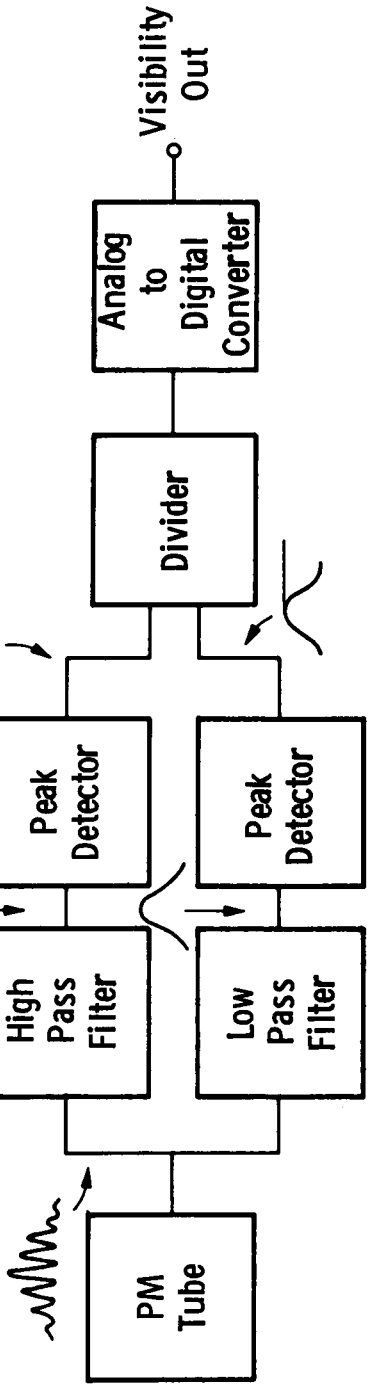


Figure 7. Visibility measurement using peak detectors.

Note that the time delay of the signal moving through the a.c. channel of the electronic circuit does not have to be the same as the time delay through the pedestal channel. Frequency response of the divider is also relatively unimportant. The peak detectors independently hold the peak value in each channel after the waveform has passed, while the divider forms the ratio of the two values.

There are disadvantages to this approach. First, a noise voltage may boost either the a.c. or the pedestal at the time the peak is recorded, giving an error in the measurement without any indication an error has occurred. Secondly, it may not be possible to adequately aperture a particular system to collect light only from the xy plane.

III. OPTICALLY APERTURED SYSTEM: INTEGRATORS

If aperturing is possible, the use of an integration method may offer greater noise rejection than peak detection. Figure 8 outlines the electronics. Once again filters separate the a.c. portion of the signal from the pedestal. This time the pedestal is integrated before it goes to the divider and the envelope of the a.c. is detected and then integrated. The output of the envelope detector is proportional to the a.c. magnitude, which is (from Equation 2-5, page 20, with z = 0):

$$V_0 \exp\left[-\frac{2}{b_0^2}\left(x^2 + y^2 \cos^2\frac{\alpha}{2}\right)\right]$$

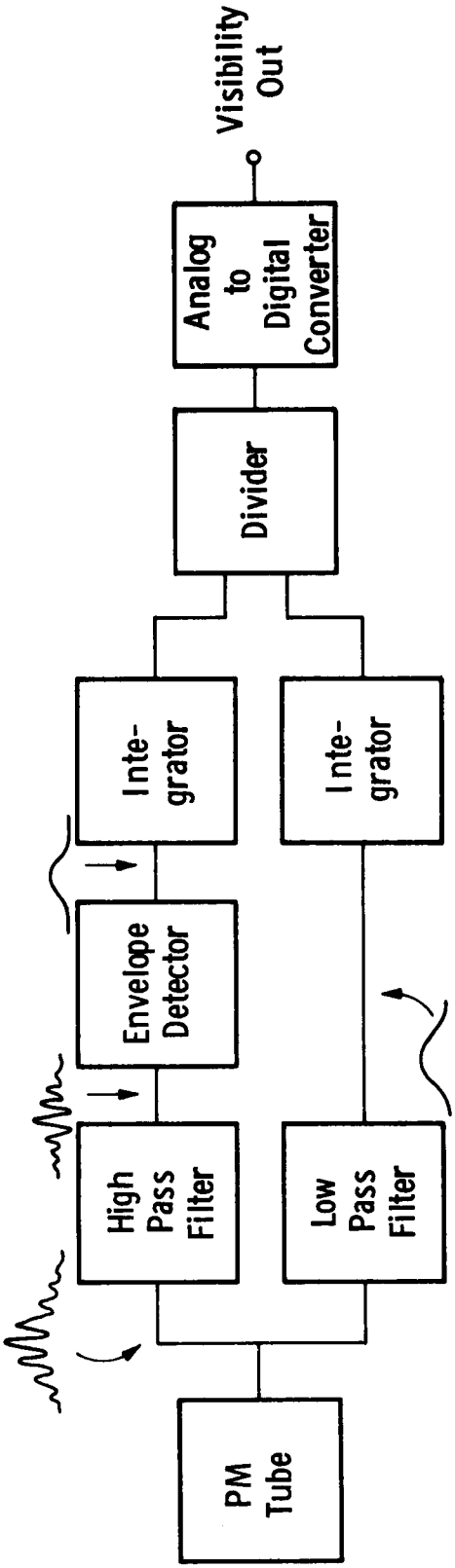


Figure 8. Visibility measurement using integrators.

The output of the divider, then, is proportional to the time integral of the a.c. magnitude divided by the integral of the pedestal:

$$\frac{V_0 \int \exp\left[-\frac{2}{b_0^2}\left(x^2 + y^2 \cos^2 \frac{\alpha}{2}\right)\right] dt}{\int \exp\left[-\frac{2}{b_0^2}\left(x^2 + y^2 \cos^2 \frac{\alpha}{2}\right)\right] dt} = V_0 \qquad (3\text{-}1)$$

The visibility as measured here depends on areas under waveforms rather than momentary values and will be less susceptible to high frequency noise voltages, although not, generally, to low frequency noise.

Use of such an integration method will increase the dynamic range of signal amplitudes within the circuit if there is a spread of particle velocities. At the divider input, the integrated signals represent areas under the waveforms rather than instantaneous values. Since the area under a Gaussian curve is proportional to its standard deviation as well as to its peak value, and since the standard deviation in this case is representative of the particle's transit time across the probe volume, the area is inversely proportional to the particle velocity. Therefore if the particles to be sized have a velocity range of 100 to 1, then the dynamic range must be increased by two orders of magnitude. For this reason the integration method would work best where there is minimal velocity variation among the particles.

IV. ELECTRONICALLY APERTURED SYSTEM

Another approach to visibility measurement which does not require an optical aperture, can be found through an examination of the visibility function. The visibility function, given by Equation 2-7, is repeated here:

$$V = \frac{V_0}{\cosh\left(\frac{2}{b_0^2}\, yz \sin \alpha\right)} \tag{2-7}$$

Since there is no dependence on x, the visibility can be plotted on the yz plane. The visibility function thus plotted looks like two long, straight levees intersecting at right angles on a flat plain. The two levees lie on the coordinate axes, and become increasingly narrow as they leave the origin. The height of the levees is V_0. Thus, when a particle traverses the probe volume, the resulting waveform reaches a maximum visibility of V_0, providing the particle crosses $y = 0$ or $z = 0$. It is tempting to consider continuously measuring the visibility throughout the particle's traversal and peak detecting it. The peak is always V_0, without regard for trajectory or aperturing, provided only that the trajectory carries the particle through either $y = 0$ or $z = 0$. It would be necessary that the peak not occur so far from probe center that it would be buried in noise. This method could also be perturbed by a momentary noise spike.

Figure 9 outlines the electronics for an alternative method which employs electronic aperturing. It is assumed that the particles move generally in the y direction. The a.c. and pedestal are again separated by filtering. The pedestal is fed directly to an analog divider and the a.c. is envelope detected, then fed to the divider. Care must be taken to match time delays through each channel and the divider must have a fast response. The output of the divider is then a continuous reading of the visibility throughout the particle's traversal.

A track and hold (sample/hold) module follows the divider. The track/hold circuit is strobed to "hold" the visibility when the a.c. peak value is reached, and the held value is digitized. A comparison circuit then monitors the subsequent output of the divider and looks for a change in the visibility (greater than some preselected value) while the particle continues its trajectory. Comparison is continued for a given length of path, say until the a.c. drops below a certain percentage of its peak value. If the visibility does not vary more than the preselected amount during the comparison period, it is assumed the particle passed through (or close to) the xy plane and the measurement is accepted as a valid measure of V_0. If the visibility varies more than the selected amount, it is assumed that either noise perturbed the signal or the particle passed too far from the $z = 0$ plane and the measurement is rejected.

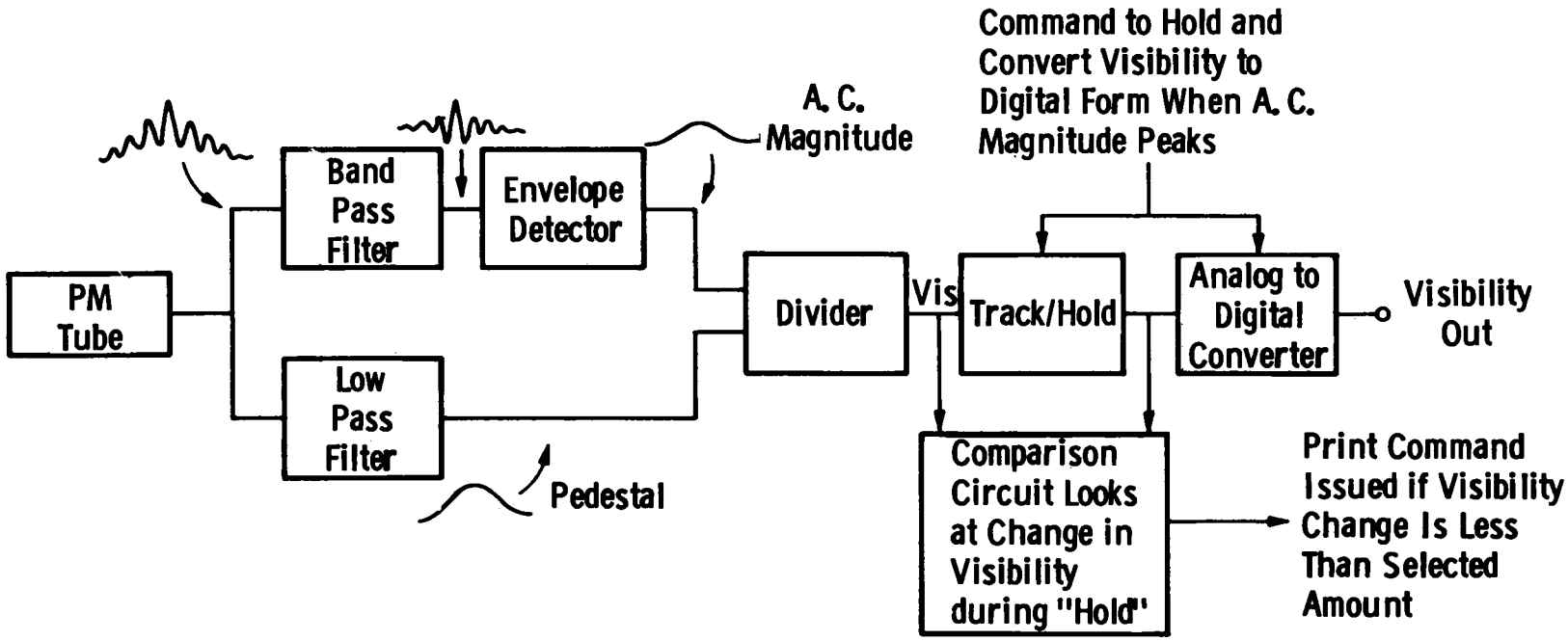


Figure 9. Visibility measurement with electronic aperturing of the probe volume.

Aperturing is thus achieved electronically and noise perturbed signals are automatically rejected.

V. VISIBILITY CHANGE DURING PARTICLE TRAVERSAL

Equation 2-7, page 21, for the visibility shows no change in the visibility as the particle travels in the $z = 0$ plane. The change in visibility from V_0 as the particle moves in the y direction through the probe volume for values of z other than zero must be known to design instrumentation using the method of electronic aperturing described above. Table I gives values of the visibility calculated from Equation 2-7, assuming $V_0 = 1$, for selected values of y and values of z near $z = 0$. The coordinates y and z have been normalized in this table so that the coordinates are equal to one at the edge of the defined probe volume (see Equations 2-3a, b, and c, page 15). The normalized variables are defined as

$$x_n = x/b_0$$

$$y_n = y \cos(\alpha/2)/b_0$$

$$z_n = z \sin(\alpha/2)/b_0 \qquad (3\text{-}2)$$

For example, $z_n = 0.2$ refers to that z coordinate which is 0.2 of the way to the z-axis intersection with the probe volume surface.

TABLE I

VISIBILITY CALCULATED FROM EQUATION 2-7 FOR SELECTED VALUES OF NORMALIZED COORDINATES y_n AND z_n

	$y_n = 0$	0.2	0.4	0.6	0.8	1.0
$z_n = 0$	1	1	1	1	1	1
$z_n = 0.050$	1	.9992	.9968	.9928	.9873	.9803
$z_n = 0.075$	1	.9982	.9928	.9840	.9719	.9566
$z_n = 0.100$	1	.9968	.9873	.9719	.9509	.9250
$z_n = 0.125$	1	.9950	.9803	.9566	.9250	.8868
$z_n = 0.150$	1	.9928	.9719	.9385	.8949	.8435
$z_n = 0.200$	1	.9873	.9509	.8949	.8252	.7477

$V_0 = 1$

From Table I for $z_n = 0.125$ it is seen that the visibility varies from V_0 at $y_n = 0$ to $0.9803\ V_0$ at $y_n = 0.4$, a change of just under 2 percent. Therefore if 2 percent were selected in the electronics as the allowable variation, and the path were monitored from $y_n = 0$ to $y_n = 0.4$, particles with a z_n coordinate exceeding ± 0.125 would be rejected. Similarly from Table I, for $z_n = 0.200$, it is seen that the visibility varies just under 5 percent from $y_n = 0$ to $y_n = 0.4$ and a 5 percent "window" monitored over this path length would pass particles for which z_n does not exceed ± 0.200.

A visibility measuring instrument which uses electronic aperturing will be described in Chapter V. In that instrument, the visibility is monitored while the particle travels from $y_n = 0$ to $y_n = 0.4$, and the measurement is rejected if the visibility varies more than 5 percent during that interval.

CHAPTER IV

FREQUENCY ANALYSIS

Methods by which the visibility could be determined electronically were investigated in Chapter III. Time and frequency domain analysis of the scattered light waveform and the waveform visibility, prerequisite for electronic design, is the subject of this chapter.

Time and frequency domain representations of laser velocimeter signals are discussed by Crosswy and Hornkohl (28) for scattering particles passing through the center of the probe volume; i.e., through the xy plane of Figure 1, page 9. The development here will be for particles passing anywhere through the probe volume as long as there is no component of velocity in the z direction, and will also include analysis of the visibility.

I. TIME DOMAIN

Equation 2-5, page 20, gives the collected scattered light intensity as a function of V_0, time t and the particle's spatial coordinates x, y and z. (The alternative Equation 2-13 for the optical signal is identical in form for our purposes here.) To obtain the current output of the photomultiplier tube as a function of time, we assume the particle moves with constant velocity, with x, y and z coordinates given by

$$x = v_x t$$

$$y = v_y t$$

$$z = z$$

Substituting these values into Equation 2-5 gives for the output current

$$i(t) \sim \exp\left[-\frac{2}{b_0^2}\left(v_x^2 t^2 + v_y^2 t^2 \cos^2\frac{\alpha}{2} + z^2 \sin^2\frac{\alpha}{2}\right)\right] \times \left[\cosh\left(\frac{2}{b_0^2} v_y t z \sin\alpha\right) + V_0 \cos(\omega_b t + 2\pi v_y t/\delta)\right]$$

which is of the form

$$i(t) = Ke^{-cz^2}e^{-at^2}[\cosh(bzt) + V_0 \cos(2\pi f_s t)] \qquad (4\text{-}1)$$

where K is a constant of proportionality and where

$$a = 2(v_x^2 + v_y^2 \cos^2(\alpha/2))/b_0^2$$

$$b = 2v_y(\sin\alpha)/b_0^2$$

$$c = 2 \sin^2(\alpha/2)/b_0^2$$

and

$$f_s = f_b + v_y/\delta$$

where f_b is the Bragg cell frequency. The a.c. frequency f_s thus is the sum of the Bragg cell frequency f_b and the rate v_y/δ at which the particle would cross stationary fringes. As a numerical example, for v_y = 10 m/s in the direction

opposite to fringe movement, δ = 50 micrometers and f_b = 15 MHz, the a.c. frequency f_s generated is 15 MHz + 0.2 MHZ = 15.2 MHz. If the particle were moving in the same direction as the fringes, the a.c. frequency observed would be 14.8 MHz.

The visibility as a function of time for particles moving parallel to the xy plane is, from Equation 2-7, page 21:

$$V(t) = \frac{V_0}{\cosh(bzt)} \qquad (4\text{-}2)$$

II. FREQUENCY DOMAIN

The Fourier transform of Equation 4-1 gives the frequency spectrum of the signal. The transform of Equation 4-2 gives the visibility spectrum. We will look first at the pedestal, then at the a.c. and finally at the visibility. In the time domain the pedestal is (from Equation 4-1)

$$i_{ped}(t) = Ke^{-cz^2}e^{-at^2}\cosh(bzt)$$

The Fourier transform may be found with the aid of integral tables (31) as:

$$I_{ped}(f) = K(\pi/a)^{1/2}\exp[-(c - b^2/4a)z^2]\exp[-\pi^2f^2/a] \times \cos(\pi bzf/a) \qquad (4\text{-}3)$$

This is a Gaussian in frequency multiplied by a cosine term. In the xy plane the cosine term is equal to one, and the

spectrum reduces to a pure Gaussian.

The pedestal bandwidth is theoretically infinite. The bandwidth can be arbitrarily defined, however, using the frequency where the envelope of the spectrum (i.e., the Gaussian factor) has decreased to 10 percent of its peak value, and the following can be noted.

1. The bandwidth is independent of the particle's z coordinate.
2. The pedestal contains frequencies extending to d.c.; i.e., to f = 0. This means the pedestal channel in the electronics must be d.c. coupled. It is true that a.c. coupling through a large capacitor would pass a single pedestal with little noticeable effect. However, removing the d.c. component of a periodic waveform causes it to "float down" until there is as much area above the time axis as there is below the time axis, and the effect on a series of random pedestals would be similar.
3. The pedestal bandwidth depends on the particle velocity. The bandwidth, designated $f_{10\%}$, may be found from the Gaussian factor in Equation 4-3 as

$$\exp[-\pi^2 (f_{10\%})^2/a] = 0.1$$

$$f_{10\%} = 0.483(a)^{1/2} \text{ Hz}$$

where as previously defined,

$$a = 2(v_x^2 + v_y^2 \cos^2(\alpha/2))/b_0^2$$

If $\cos(\alpha/2) \simeq 1$, then

$$f_{10\%} = 1.37\ v_p/2b_0 \text{ Hz} \qquad (4\text{-}4)$$

where v_p is the particle velocity.

The a.c. component in the time domain is (from Equation 4-1)

$$i_{ac}(t) = Ke^{-cz^2}e^{-at^2}V_0 \cos(2\pi f_s t) \qquad (4\text{-}5)$$

and the Fourier transform is

$$I_{ac}(f) = (KV_0/2)(\pi/a)^{1/2}\exp[-cz^2] \times \{\exp[-\pi^2(f + f_s)^2/a] + \exp[-\pi^2(f - f_s)^2/a]\} \qquad (4\text{-}6)$$

This is composed of two Gaussians, one on the positive frequency axis centered at f_s, the other on the negative frequency axis centered at $-f_s$. Except for the translation in frequency and a magnitude factor, each Gaussian is identical to the pedestal spectrum Gaussian factor. The bandwidth, then, of the a.c. component is twice the bandwidth of the pedestal.

Figure 10 illustrates the positive frequency portion of the magnitude of the pedestal and a.c. spectra for two cases: (1) the particle passes through the center of the

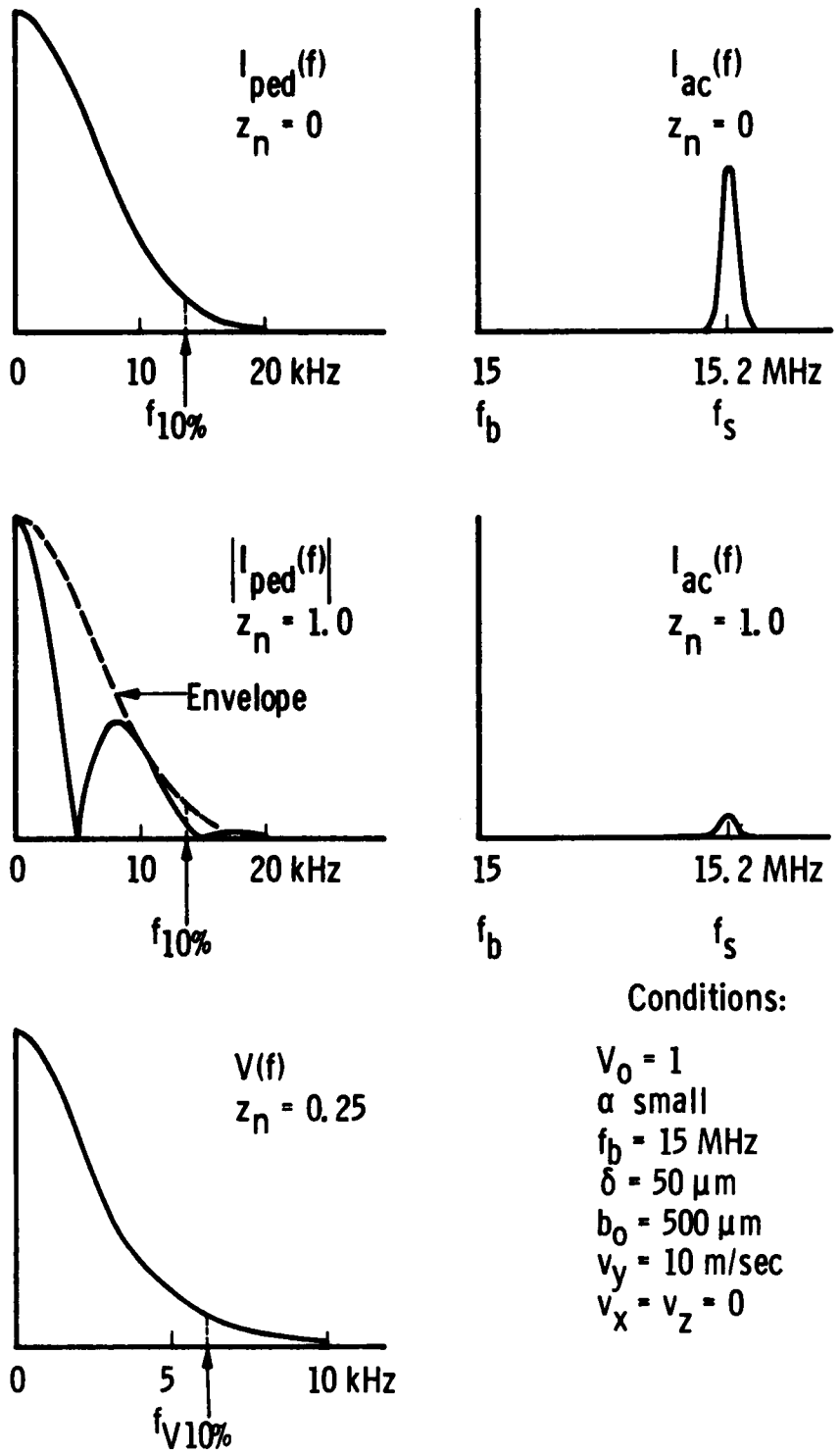


Figure 10. Frequency spectra: pedestal and a.c. for $z_n = 0$, 1.0; visibility for $z_n = 0.25$.

probe volume ($z = 0$), and (2) the particle passes at the edge of the probe volume ($z = b_0/\sin(\alpha/2)$). Other conditions used in making the plots are shown on Figure 10. It can be seen that electronic filtering can be used to separate the a.c. from the pedestal, provided the a.c. frequency f_s is sufficiently large compared to the spectra bandwidths which are in turn proportional to particle velocity.

The frequency domain representation of the visibility, found by Fourier transforming V(t) given by Equation 4-2, is

$$V(f) = \frac{V_0 \pi}{bz} \frac{1}{\cosh(\pi^2 f/bz)}, \quad |z| > 0 \tag{4-7}$$

(For $z = 0$, the visibility is a constant, equal to V_0, and the frequency spectrum is an impulse at $f = 0$.) The bandwidth of the visibility signal can be defined in a manner similar to that done for the pedestal; i.e., as that frequency where the spectrum has decreased to 10 percent of its peak value.

The visibility bandwidth $f_{v10\%}$ thus defined is found as

$$\cosh[\pi^2 (f_{v10\%})/bz] = 10$$

$$f_{v10\%} = 0.303\ bz \quad \text{Hz} \tag{4-8}$$

where, as defined previously,

$$b = \frac{2}{b_0^2} v_y \sin \alpha$$

Unlike the pedestal bandwidth (Equation 4-4), the visibility bandwidth is dependent on the z coordinate. Figure 10, page 53, includes a plot of the visibility spectrum for a particle passing with a z coordinate one-fourth of the way from probe center to the edge of the probe volume ($z_n = 0.25$).

CHAPTER V

SIGNAL PROCESSOR FOR VISIBILITY MEASUREMENT

As part of the research reported here, an electronic signal processor was designed and constructed for use with an optical interferometer to read out the signal visibility v_0, from which particle size can be determined. The method used employs electronic aperturing as described in Chapter III, wherein the visibility is measured continuously to look for particles whose visibility has minimal variation, indicating particle passage near probe center. The processor was designed for use with an interferometer using a Bragg cell driven at 15 MHz. Figure 9, page 44, is a simplified block diagram of the electronics.

I. SIGNAL BANDWIDTHS

Frequency response limitations encountered in the control circuit development require limiting the particle time in the probe volume, that is, a time equal to $2b_0/v_p$, to a minimum of 65 microseconds. This establishes the maximum allowable pedestal signal bandwidth (through Equation 4-4) to be

$$f_{10\%} = 21.0 \text{ KHz} \qquad (5\text{-}1)$$

and the pedestal channel response should be flat to this frequency.

The a.c. spectrum is a Gaussian in frequency of bandwidth $2f_{10\%}$, centered on f_s as discussed in Chapter IV and illustrated in Figure 10, page 53. The center frequency f_s is given by (see Equation 4-1)

$$f_s = f_b + v_y/\delta$$

where f_b is the Bragg cell frequency, here equal to 15 MHz, δ is the fringe spacing and v_y is the particle velocity, assumed here to be opposite the direction of fringe movement. The a.c. channel frequency response should be flat over the expected range of $(f_s \pm f_{10\%})$. For velocity v_y varying from zero to a maximum of 15m/sec, and with a minimum fringe spacing δ = 50 micrometers, the corresponding range of f_s is from 15.0 MHz to 15.3 MHz, and the maximum expected a.c. signal bandwidth of $2f_{10\%}$ = 42.0 KHz does not substantially add to this. Therefore, the a.c. channel is required to pass without attenuation only frequencies from approximately 15.0 MHz to 15.3 MHz, a very narrow range.

The frequency response of the divider and of the signal circuit beyond the divider should extend to beyond the bandwidth $f_{v10\%}$ given for the visibility by Equation 4-8. This bandwidth is proportional to the spatial coordinate z. However, values of normalized coordinate z_n (z_n = $z \sin(\alpha/2)/b_0$) greater than say 0.25 do not have to be considered because electronic aperturing can be used to reject particles with $z_n > 0.25$ (see Chapter III). For z_n = 0.25, α small and the ratio $2b_0/v_y$ = 65 microseconds, Equation 4-8

gives for the required bandwidth

$$f_{v10\%} = 9.32 \text{ KHz} \qquad (5\text{-}2)$$

The remainder of this chapter will describe the processor in two parts: (1) the signal processing circuit, and (2) the control circuit. The control circuit determines when the peak of the a.c. is reached, starts the visibility measurement, and then rejects those signals where the visibility varies more than the selected amount or where the signal amplitude is outside the capability of the signal processing circuit to handle. The control circuit also provides a print command for an external recording device if the visibility measurement is acceptable, and resets the processor after signal passage.

II. SIGNAL PROCESSING CIRCUIT

First-Stage Amplification

Referring to Figure 11, first-stage amplification employs a Fairchild uA733 wide-band integrated circuit amplifier, designated on the diagram as 733-1. The uA733 has a frequency response specified to extend to 100 MHz. (The frequency response of this amplifier and of the other components used was checked and found to be flat ±1 percent over the applicable ranges as part of the benchcheck described in Chapter VI.) The gain may be varied over a range of approximately 10 by connecting a 10K ohm potentiometer across terminals 3 and 12 as shown. The 733-1 is

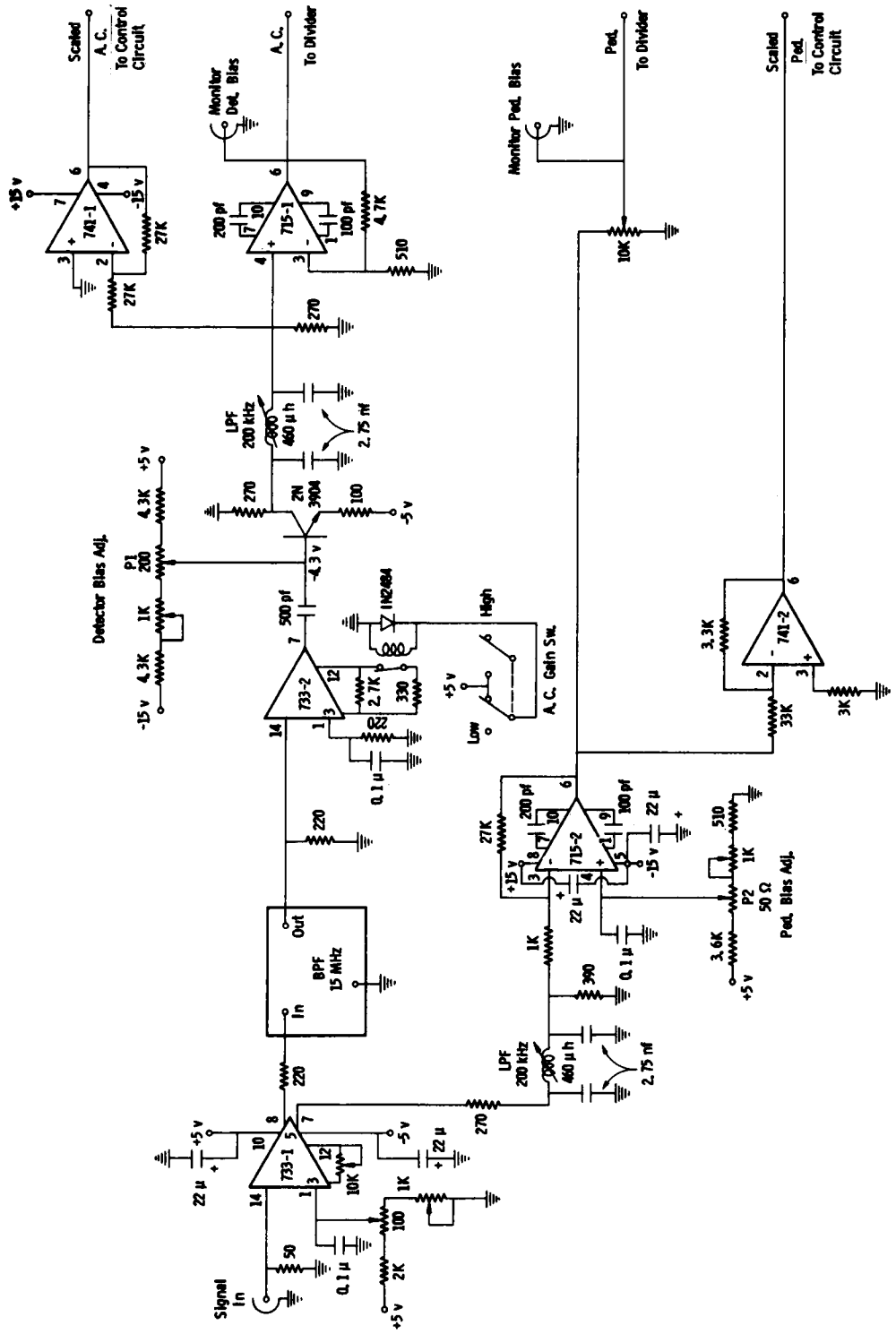


Figure 11. Signal processing circuit, part I.

coupled directly into the circuit, as are all the pedestal circuit paths, since capacitive coupling would block direct currents and the pedestal signal contains frequency components down to d.c. (f = 0). The amplifier has a differential input and both inverted and non-inverted outputs. The signal input is taken from a front panel connector; the opposite input is taken from a variable voltage divider to offset signal input d.c. bias. One amplifier output (pin 8) goes to the a.c. channel and the other output (pin 7) goes to the pedestal channel. Maximum uA733 signal output was found experimentally to be approximately 1500 millivolts, zero to peak, when driving 200 ohms or more.

Pedestal Channel Low Pass Filter

The pedestal component of the signal (from pin 7 of the 733-1) passes through a 200 KHz low pass filter, which removes the a.c. component and acts as a noise filter. It is a standard design, third-order filter with a theoretical fall-off of 18db/octave beyond the -3db frequency. The source resistance for the filter is the series combination of the 270 ohm resistor and the 20 ohm output resistance of the 733-1. The filter's matching load resistance is provided by the parallel combination of the 390 ohm and 1K ohm resistors. The filter's frequency response was measured flat ±1 percent from d.c. to beyond 50 KHz. Time delay through the filter was measured to be 1.8 microseconds.

A.C. Channel Band Pass Filter

The a.c. component of the signal passes through a 15 MHz sharp cut-off band pass filter which removes the pedestal and acts as a noise filter. The filter used is a T.T. Electronics, Inc., Model K17C. Its frequency response was measured flat ±1 percent from 15.0 MHz to 15.6 MHz. Attenuation was a measured 40 db at 12 MHz and 34 db at 20 MHz, although attenuation was only 20 db in the range from 40 MHz to 100 MHz.

A.C. Channel Gain Selection

A second uA733 amplifier, designated 733-2 in Figure 11, page 59, is used in the a.c. channel downstream of the band pass filter to recover gain lost in the filter. Either of two fixed gains for this amplifier (the "high" gain is 2.5 times greater than the "low" gain) is selectable by a front panel switch, which connects either of two resistance values across the amplifier's gain terminals. The same switch simultaneously selects voltage dividing further downstream (just beyond the divider) to keep the overall a.c. component gain balanced with the gain provided the pedestal. The purpose of the selectable higher a.c. channel gain is to boost small a.c. signals associated with low visibilities into a more suitable amplitude range for the a.c. channel envelope detector.

A.C. Channel Envelope Detector

The envelope of the a.c. signal is extracted using an amplitude modulation detector. The 2N3904 transistor of Figure 11, page 59, used in the common emitter configuration, is biased near cut-off to act as a half-wave rectifier and is followed by a low pass filter.

The input bias voltage for the 2N3904 is provided by a voltage divider (P1) which was adjusted experimentally for optimum linearity of the detector output. Supply voltage for the 2N3904 was chosen to give a collector output bias voltage near ground potential.

The 200 KHz low pass filter is identical to the one at the input to the pedestal channel, since the envelope of the a.c. requires the same frequency bandwidth as the pedestal, and since it is desired to equalize time delays through each channel.

Figure 12 plots the output of the envelope detector, measured at the a.c. channel output, versus the input. It is linear within 5 percent over a 10:1 amplitude range; i.e., for outputs from -450 mv to -4.5 volts. The input plotted in Figure 12 is measured at the input to the uA733-2. It can be seen that the output, below the linear range, levels out and is equal to -200 mv for zero signal input. This bias was chosen experimentally for best linearity. The output that exists when the signal is zero, i.e., -200 mv, when applied to the numerator input of the divider, causes

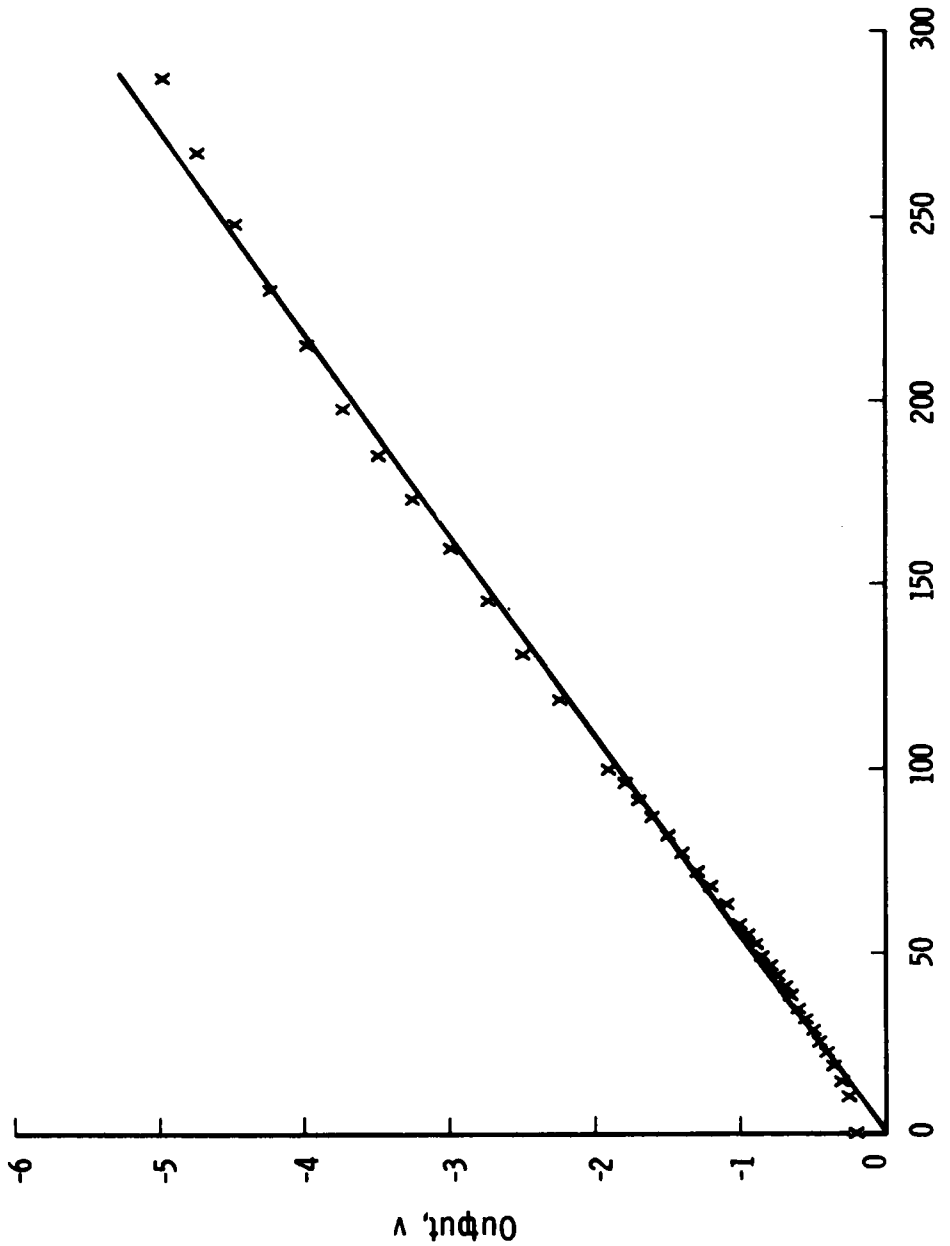


Figure 12. A.C. envelope detector response.

the divider output to saturate at +12 volts when the input signal is zero.

The operation of the detector used here can be explained in terms of the 2N3904 being modeled as a half-wave rectifier. The input to the 2N3904 is of the form

$$V_{in}(t) \sim e^{-at^2} \cos \omega_s t$$

The output of the 2N3904 is the half-wave rectified version of this:

$$v_0(t) \sim e^{-at^2} [\cos \omega_s t]_{rect}$$

The frequency spectrum of this output can be written as the Fourier transform of $\exp(-at^2)$ convolved with the Fourier transform of a half-wave rectified cosine wave:

$$\mathcal{F}\{v_0(t)\} = \mathcal{F}\{e^{-at^2}\} * \mathcal{F}\{[\cos \omega_s t]_{rect}\}$$

The transform of a periodic signal is a series of impulses in frequency, the weights of the impulses given by the coefficients of the exponential Fourier series representing the signal. The Fourier series for a periodic, half-wave rectified cosine is (see for example Reference (32), page 193):

$$[\cos \omega_s t]_{rect} = (1/\pi) + (1/2) \cos \omega_s t + (2/3\pi) \cos 2\omega_s t - (2/15\pi) \cos 4\omega_s t + \cdots$$

$$= \cdots -(1/15\pi)e^{-i4\omega_s t} + (1/3\pi)e^{-i2\omega_s t}$$
$$+ (1/4)e^{-i\omega_s t} + (1/\pi) + (1/4)e^{i\omega_s t}$$
$$+ (1/3\pi)e^{i2\omega_s t} - (1/15\pi)e^{i4\omega_s t} + \cdots$$

Therefore, the transform is

$$\mathcal{F}\{[\cos \omega_s t]_{rect}\} = \cdots -(1/15\pi)\delta(f + 4f_s) + (1/3\pi)\delta(f + 2f_s)$$
$$+ (1/4)\delta(f + f_s) + (1/\pi)\delta(f)$$
$$+ (1/4)\delta(f - f_s) + (1/3\pi)\delta(f - 2f_s)$$
$$- (1/15\pi)\delta(f - 4f_s) + \cdots$$

where $\delta(f + 4f_s)$ is an impulse located at $-4f_s$ on the frequency axis, etc., and $f_s = \omega_s/2\pi$.

The transform of $\exp(-at^2)$ is a Gaussian whose bandwidth has been defined by Equation 4-4. Convolving this transform with the series of impulses in frequency representing the rectified cosine simply reproduces the Gaussian at each point in frequency where there is an impulse (and multiplies it by the area under the impulse).

This result is the spectrum of the half-wave rectified output of the 2N3904. The following low pass filter passes only the Gaussian centered at zero frequency, which in the time domain is the desired envelope, $\exp(-at^2)$.

Pedestal and A.C. Channel Operational Amplifiers

Both channels are terminated by high slew rate Fairchild uA715 operational amplifiers, designated 715-1 and

715-2 in Figure 11, page 59, to amplify the signals for input to the analog divider. The uA715 has a unity gain bandwidth specified greater than 10 MHz and a minimum slew rate of 15 volts/microsecond.

The a.c. channel uses a non-inverting configuration for this amplification stage, with a gain of 10. The pedestal uses an inverting stage with a gain of 23. A variable voltage divider (P2 in Figure 11) provides front panel-adjustable bias to the non-inverting input of the pedestal op-amp to zero its output bias. Both a.c. and pedestal are passed inverted to the divider. The divider specifies a negative denominator input, and since a positive divider output is desired, both divider inputs are made negative.

The processor's control circuit requires non-inverted versions of the a.c. and pedestal, scaled down by a factor of 10. The "scaled a.c." and "scaled pedestal" signals are made available for this purpose by general purpose uA741 op-amps, designated 741-1 and 741-2, respectively (see Figure 11), used in the inverting configuration.

Equalizing Pedestal and A.C. Gains

To correctly measure the ratio of the a.c. to the pedestal requires that both components receive equal gain (or that their relative gains be known). The total gain provided the a.c. component from the processor input to the numerator input of the analog divider was measured to be 56.

This was measured with the a.c. gain selector (on the uA733-2) set to the low position. (As described previously, setting the a.c. gain to high increases a.c. gain by a factor of 2.5 to boost small a.c. signals associated with low visibilities into the linear range of the envelope detector. Selecting high a.c. gain simultaneously selects voltage dividing just beyond the divider to multiply the divider output by 1/2.5.) The continuously variable uA733-1 gain was also set at minimum when the measurement was made. Increasing the 733-1 gain to maximum increases the gain of the total signal, a.c. and pedestal, by approximately a factor of 10. The total gain provided the pedestal component was adjusted to 56.0 to match the a.c. gain, by adjusting a voltage dividing potentiometer at the output of the pedestal channel.

Equalizing Pedestal and A.C. Channel Time Delays

Time delays through each channel are determined primarily by the relatively long delays through the two low pass filters. The delay through each low pass filter is approximately 1.8 microseconds. Small screw adjustments were made to the filter inductors to equalize the time delays, without appreciably affecting the frequency response of the filters.

Analog Divider

The a.c. component is divided by the pedestal in the analog divider (Figure 13), giving the visibility at the

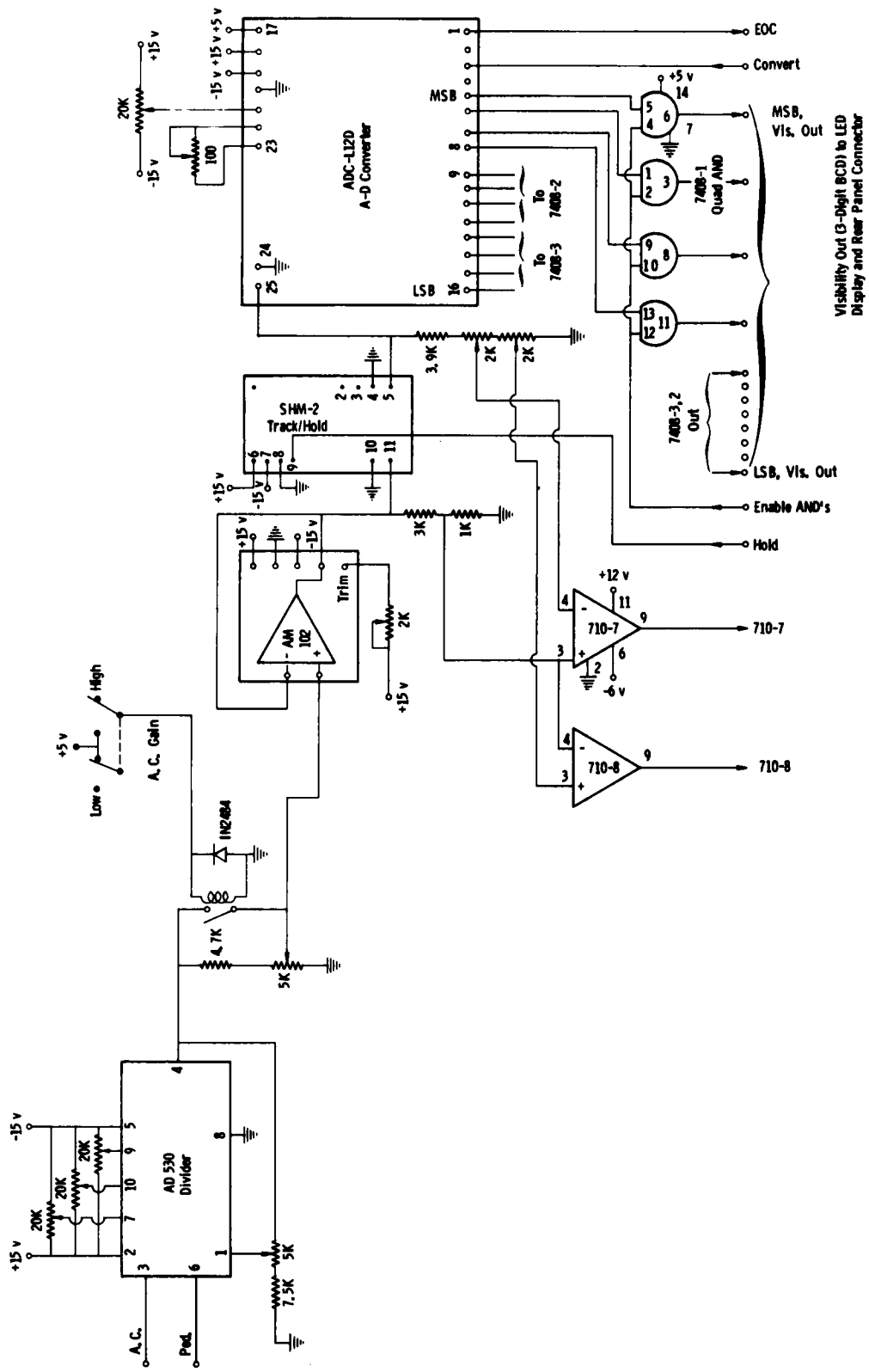


Figure 13. Signal processing circuit, part II.

divider output. The divider used is an Analog Devices, Inc., integrated circuit Model AD530. The divider is specified to have a 3 db bandwidth of 750 KHz when the denominator is -10 volts and 75 KHz when the denominator is -1.0 volt. The divider output over its linear range is equal to 10(N/D) volts where N is the numerator and D the denominator; i.e., for N equal to D, the output is 10 volts. A visibility equal to 1.00, then, corresponds to a divider output of 10.0 volts. The divider's performance was checked as described in Chapter VI.

Track-Hold Circuit

Following the divider is a track-hold (sample-hold) circuit whose function is to hold the value of the visibility upon command from the processor's control circuit. The value is held while it is converted to digital form by the following analog-to-digital converter, and while the value is compared by the control circuit with the subsequent visibility output by the divider. This circuit is composed of a high speed voltage-following op-amp and a fast, Datel Systems Model SHM-2 sample-hold module. The op-amp, a Datel Systems Model AM-102, has a specified bandwidth of 2 MHz and a slew rate of 140 volts/microsecond when used as a follower, and is recommended by Datel as an input buffer for the SHM-2. The SHM-2 sample-hold has a specified 3 db bandwidth of 500 KHz.

Visibility Variation Window

Either of two uA-710 comparators, designated 710-7 and 710-8 in Figure 13, provides a logic "1" voltage level to the processor control circuit if the visibility varies more than a selected amount after the "hold" command is given to the sample-hold. Referring to Figure 13, page 68, the visibility output by the AM-102 op-amp is scaled down through a voltage divider following the op-amp, and is applied to pin 3, 710-7, and to pin 4, 710-8. Potentiometers in a voltage divider following the sample-hold module were adjusted to select values 5 percent above and below this value for comparison with it. With the sample-hold in the hold mode, if the op-amp output varies as much as the selected percentage, the output of either the 710-7 or the 710-8 will go to a logic 1, depending on which way the variation occurred.

Analog-to-Digital Converter

A "convert" command is supplied to the Datel Systems Model ADC-L analog-to-digital (A-D) converter (Figure 13, page 68) by the processor's control circuit at the same time the track-hold circuit is signaled to hold. The converter analog input (ranging from zero to +10 volts) is converted to a three-digit, binary-coded-decimal (BCD) output in 16 microseconds. The output is at transistor-transistor logic (TTL) voltage levels.

Visibility Read-Out

A three-digit, light-emitting diode (LED) display on the processor front panel displays the measured signal visibility if the control circuit determines that a valid measurement was made. Logic "AND" gates (Figure 13, page 68) between the A-D converter output and the LED display pass the measured visibility only if an "enable" signal from the control circuit enables them. There are 12 AND gates required, one for each bit comprising the three-digit BCD output. Three type 7408 quadruple AND gates are used, only one of which is shown in Figure 13 in order to simplify the diagram.

The BCD output is also made available at the rear of the processor along with a "print" command, for an external recording device such as a printer.

III. CONTROL CIRCUIT

Before describing the processor control circuit and its operation, a brief description will be given of the digital integrated circuits used in this portion of the processor. Transistor-transistor logic (TTL) is used.

NAND Gates

Two type 7400 quad NAND gates are used. Four independent, two-input NAND gates are in each 7400 package. Only when both inputs of a NAND gate are high is the output low. Gates which are part of one 7400 are designated on the

circuit diagram as 00-1A, B, C and D; gates belonging to the other 7400 are designated 00-2A, B, C and D.

NOR Gates

Three 7402 quad NOR gates are used. When either or both inputs of a NOR gate are high, the output is low. NOR gates are identified on the diagram as belonging to a particular 7402 package by 02-1, 02-2, or 02-3, with suffixes A, B, C and D.

One-Shots

Two types of "one-shot" multivibrator are used, the type 9601 and the type 74121. Both are similar in operation. The 9601 produces a single positive pulse at pin 8 and a negative pulse at pin 6. Pulse duration depends on the values of external timing resistor and capacitor used. The 74121 produces positive and negative pulses at pins 6 and 1, respectively. Proper conditions must be met at the inputs of these integrated circuits before the output pulse is produced. The 9601 requires both pins 3 and 4 to be high (logic 1) and simultaneously requires either or both pin 1 and pin 2 low (logic 0). The 74121 requires pin 5 high and either or both pin 3 and pin 4 low.

Flip-Flops

The operation of the type 7473 dual JK "flip-flops" as they are wired in this circuit may be described as follows. A momentary low at the R input resets the Q output

low and the $\overline{Q}$ output high. When the clock (C) input falls from high to low, Q goes high and $\overline{Q}$ goes low; the flip-flop is then disabled until reset.

In addition to the two 7473 JK flip-flops used, the two NAND gates designated 00-2B and 00-2C are wired as a reset-set (RS) latch, which is a basic flip-flop. If a momentary low is applied to pin 9 of this combination, which is the "set" terminal, the Q output (pin 8) goes high and $\overline{Q}$ (pin 11) goes low. If a momentary low is then applied to pin 13, which is the "reset" terminal, Q returns low and $\overline{Q}$ goes high.

Comparators

Comparators are classified as linear devices, rather than digital. A number of uA710 comparators are used in the circuit. One uA760 comparator, similar to, but faster than the uA710, is used in the peak detector circuit where faster operation is desired. If the "+" input of a comparator is more positive than the "-" input, the output goes to a logic "1," and vice versa. The comparators used do not have the capability of driving more than two TTL gates. Therefore, in this circuit most of the comparators are followed by a 7402 NOR gate buffer, simply wired as an inverter. The 7402 has greater current capability and can drive as many as 10 gates.

Signaling A.C. Peak Passage

A requirement of the method of visibility measurement outlined in Figure 9, page 44, and being implemented here, is to know the time when the a.c. reaches its peak value so that commands can be given to the sample-hold and the analog-to-digital converter to hold and convert the value of the visibility there. That part of the control circuit shown in Figure 14 performs this function.

Referring to the small sketch in the lower right of Figure 14, this circuit is used to generate two signals: (1) a signal designated "a.c. pk." which follows the rising side of the scaled a.c. and then holds the peak value reached, and (2) a signal designated "a.c. sig." which is simply the scaled a.c. multiplied by 1.1 in an op-amp. These two waveforms are in turn utilized by a comparator to signal the time when the a.c. sig. falls below the a.c. pk., indicating peak passage.

The a.c. sig., being 10 percent larger than the scaled a.c., climbs faster and remains above the a.c. pk. while the two signals are rising. When the a.c. sig. starts to fall at peak passage, however, it rapidly crosses and falls below the peak value held by the a.c. pk. The a.c. sig. and the a.c. pk. are fed into a uA710 comparator, designated 710-1 in Figure 14, followed by a NOR gate (02-1A) used as an inverting buffer, whose output switches from logic 0 to logic 1 when this crossing occurs.

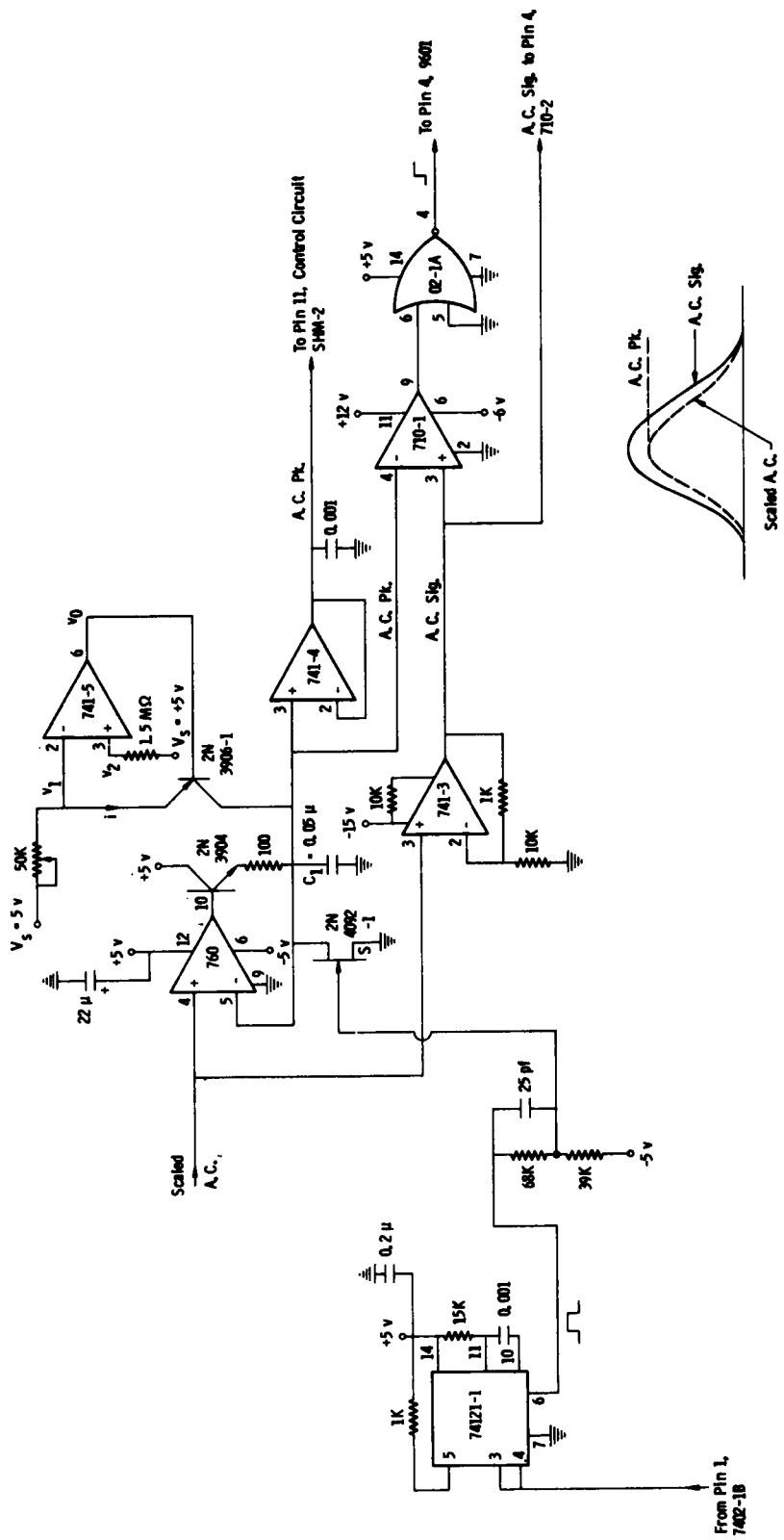


Figure 14. Control circuit, part I.

Peak Detector

The uA760 comparator, 2N3904 and 2N3906-1 transistors and the uA741-5 op-amp shown in Figure 14 are used to form a peak-detecting circuit. The input to this circuit is the scaled a.c., which is applied to pin 4 of the 760. The output, which is the a.c. pk. signal, appears at the non-grounded side of the 0.05 microfarad storage capacitor (C1 in Figure 14). From there the a.c. pk. goes directly to the 710-1 comparator and is also made available to a following portion of the control circuit through the uA741-4 op-amp used as a voltage following buffer.

The operation of the peak detector circuit is as follows. When the input to the 760 comparator (pin 4) is more positive than the voltage on the storage capacitor (which is fed back to the "-" input of the 760), the comparator output goes high to +3.2 volts, which turns on the 2N3904 transistor. The 2N3904 emitter current fills the storage capacitor until the voltage on the storage capacitor is equal to the input at pin 4, whereupon the comparator goes low (to ground potential), turning the 2N3904 off. This on-off cycle occurs many times while an input signal is climbing, but when an input signal reaches its peak and starts falling, the 760 output remains low, the 2N3904 remains turned off, and the peak voltage value reached by the input signal remains on the storage capacitor.

The 2N3904 transistor is not required for basic circuit operation. However, it increases the ability of the

peak detector to follow fast rising signals because of the greater current available from the transistor than directly from the comparator output. The 100 ohm emitter resistance value was chosen experimentally for fast operation with minimum oscillation of the output voltage.

The voltage stored on the storage capacitor C1 slowly bleeds off. The greatest drain on this capacitor is the input bias current into pin 5 of the comparator, which varies with the differential input voltage to the comparator and can be greater than 10 microamperes.

Constant Current Source

The uA741-5 and 2N3906 in Figure 14, page 75, form a constant current source input to the storage capacitor C1 designed to partially compensate for the bias current drain to the comparator. The current source is adjustable by the 50K ohm potentiometer shown, but cannot be used to exactly cancel the capacitor drain because of the dependence of the bias current on comparator input voltage. Instead, the current source is adjusted experimentally to reduce the current drain on the capacitor and the consequent voltage droop in the a.c. pk. signal.

Referring to the circuit diagram of the constant current source (Figure 14), equations governing its action are:

$$v_0 = -A_{01}(v_1 - v_2)$$

$$v_1 = v_0 + v_{EB}$$

$$i_s \simeq (V_s - v_1)/R$$

where v_1 and v_2 are the input voltages to the op-amp as shown in Figure 14, page 75, A_{01} is the op-amp open loop gain, v_0 is the op-amp output voltage, v_{EB} is the 2N3906 transistor emitter-to-base voltage, V_s is the supply voltage which is equal to +5 volts, R is the value of resistance set by the 50K ohm potentiometer and i_s is the current provided by the source.

Substituting the value of v_0 given by the first equation into the second equation gives

$$v_1 = -A_{01}(v_1 - v_2) + v_{EB}$$

$$= \frac{A_{01}}{1 + A_{01}} v_2 + \frac{1}{1 + A_{01}} v_{EB}$$

Because $A_{01} >> 1$, $v_1 \simeq v_2$, with variations in v_{EB} having negligible effect.

The voltage v_2 is established by the input bias current of the op-amp flowing through the 1.5 Meg ohm resistor at the pin 3 input to the op-amp. The input bias current of a uA741 op-amp is typically 100 nanoamperes, giving $v_2 = 4.85$ volts. Substituting this value of v_2 for v_1 in the third of the three governing equations above gives

$$i_s \simeq 0.150/R$$

For example, to obtain a constant current of 10 microamperes, R should be set to 15K ohms.

The 74121-1 one-shot and the 2N4092 junction field effect switching transistor shown in Figure 14 form a circuit used to discharge the peak detector storage capacitor after signal passage. When the signal has passed, the input to pins 3 and 4 of the one-shot goes low. This low originates at the output of gate 7402-1B, to be discussed later. When pins 3 and 4 go low, a positive 5 volt, 10 microsecond pulse is produced at pin 6 which causes the 2N4092 transistor to turn on. The "on" resistance of the field effect transistor is about 50 ohms, discharging the 0.05 microfarad capacitor C1 with a time constant RC equal to 2.5 microseconds. At the termination of the 10 microsecond pulse, the 2N4092 is turned off. Therefore, the 10 microsecond pulse discharges the capacitor for four time constants after signal passage, preparing it to measure the next signal peak.

Convert Command

One function of the circuit of Figure 15 is to generate the "convert" command, which is delivered to the analog-to-digital converter when certain conditions are met. These conditions are as follows:

1. The signal labeled a.c. sig. must be greater than 110 mv, corresponding to the a.c. component being greater than 1.0 volt at the divider input,

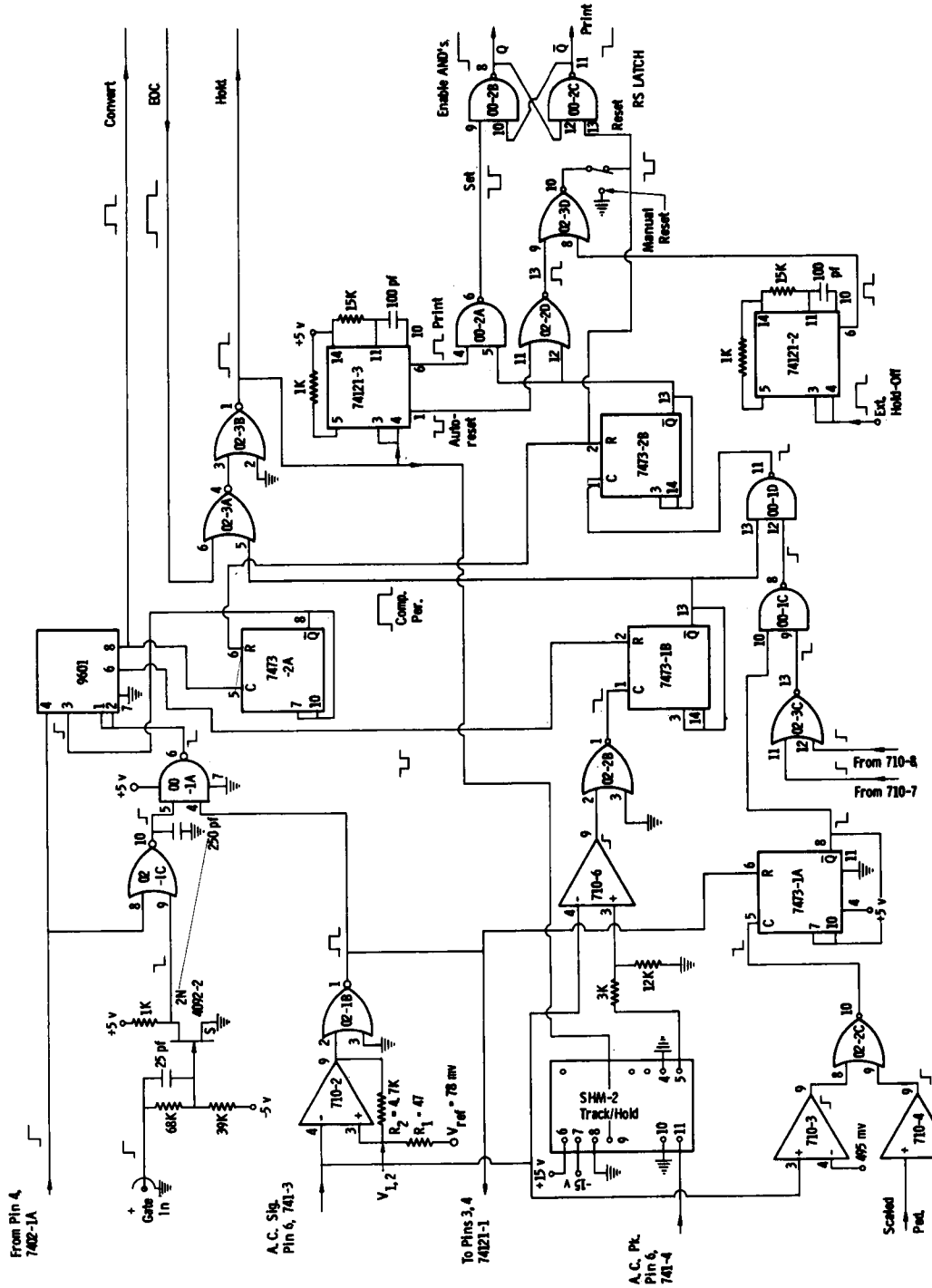


Figure 15. Control circuit, part II.

having risen far enough into the linear range of the envelope detector for a valid visibility measurement. This also assures that the pedestal component, which is never less than the a.c. component, has also reached 1 volt at the divider's denominator input, which is required for best divider accuracy and frequency response. When the a.c. sig. goes above 110 mv, the output of gate 02-1B shown in Figure 15 goes high. The hysteresis wired into this part of the circuit will be discussed in a later paragraph.

2. A "+gate" voltage of 5.0 volts or more must be available at a front panel connector, from an oscilloscope monitoring the processor input waveform. This +gate voltage is generated by an oscilloscope only for the duration of each scope sweep, and does not appear until the scope triggers on the input waveform. This allows synchronizing the scope and processor so that the same waveform for which the processor measures visibility will be displayed for comparison on the oscilloscope screen. When the +gate input to the processor goes to +5 volts, the 2N4092-2 transistor (Figure 15) is turned on and the voltage at this transistor drain goes to approximately ground potential, creating a logic "0."

3. The processor must be "enabled" by the $\overline{Q}$ terminal (pin 8) of flip-flop 7473-2A (Figure 15, page 80) high. The processor is disabled by the convert command itself, after it is generated by the convert command's "clocking" the C input of 7473-2A to cause the $\overline{Q}$ output to go from high to low. The processor remains disabled while the visibility is measured and the result read out. The processor is then reenabled by a momentary low being applied to the R terminal (pin 6) of the 7473-2A, resetting it.
4. The a.c. sig. must be greater than the a.c. pk. signal. This condition exists while the a.c. is rising (before the peak occurs), and until the a.c. sig. falls below the a.c. pk. immediately after peak passage. This condition is imposed to ensure that the convert signal cannot be given at some point on the waveform later than peak passage. The output of gate 02-1A (Figure 14, page 75) is low while this condition is met. This condition is retained for a short length of time (the delay time through two gates, about 20 nanoseconds) at the output of 00-1A (Figure 15) after the actual time the a.c. sig. falls through the a.c. pk.
5. When all four of the above conditions are met on the rising side of the a.c. component waveform,

the fifth and final condition necessary to issue the convert command is the falling of the a.c. sig. below the a.c. pk. This results in a high at the output of 02-1A. Although this condition and condition number four, above, are mutually exclusive, condition four is retained momentarily at the output of 00-1A, long enough to exist simultaneously with condition five, and the convert command is generated. The convert command is a one microsecond positive pulse delivered to the A-D converter from pin 8 of the 9601. It is produced when the five conditions listed above are simultaneously applied as shown in Figure 15, page 80, to input pins 1, 2, 3 and 4 of the 9601.

Returning to condition one above, it was noted that when the a.c. sig. goes above 110 mv, the output of 02-1B goes high. This follows the output of comparator 710-2 going low. Resistors R_1 and R_2 shown in Figure 15 at the 710-2 provide a hysteresis effect. This means the a.c. sig. input to pin 4 of 710-2 must rise to some voltage V_1 for the 710-2 output to swing low (to -0.5 volts) but must then fall to a voltage V_2 less than V_1 for the output to swing back high to 3.2 volts. The resistors R_1 and R_2 act as a voltage divider between the 710-2 output and the reference voltage designated V_{ref} in Figure 15.

The equations for this voltage divider are:

$$\frac{V_1 - V_{ref}}{R_1} = \frac{3.2 - V_{ref}}{R_1 + R_2} \quad \text{(710-2 output high)} \qquad (5\text{-}3)$$

$$\frac{V_2 - V_{ref}}{R_1} = \frac{-0.5 - V_{ref}}{R_1 + R_2} \quad \text{(710-2 output low)} \qquad (5\text{-}4)$$

Solving simultaneously for $V_1 - V_2$ to find the separation between these values gives

$$V_1 - V_2 \simeq 3.7\ R_1/(R_1 + R_2) \text{ volts}$$

In this circuit, R_1 and R_2 were chosen to be 47 ohms and 4.7 K ohms, to give a separation of V_1 and V_2 (hysteresis) equal to about 37 mv.

Using Equation 5-3 above, for V_1 to be the desired 110 mv, V_{ref} must be

$$V_{ref} = V_1\left(\frac{R_1 + R_2}{R_2}\right) - 3.2\ R_1/R_2$$

$$\simeq 78 \text{ mv}$$

Subtracting the hysteresis from V_1 gives

$$V_2 = 110 - 37 = 73 \text{ mv}$$

Hysteresis is used at this comparator because the output of the following gate, 02-1B, is connected to the 74121-1 one-shot of Figure 14, page 75, in order to discharge the peak detector storage capacitor. This should occur after the visibility measurement is completed, and

hysteresis is used here to delay the time when the 02-1B output goes low.

Hold Command

When the A-D converter begins conversion, it in turn outputs an "end-of-conversion" (EOC) pulse. This is a positive pulse which remains high until conversion is complete. This EOC pulse passes through an OR gate (made up of the combination of 02-3A and 02-3B, Figure 15, page 80) to produce the positive "hold" command for the sample-hold module. (The hold signal is also applied to a second sample-hold module, used in the control circuit and to be discussed shortly.) The opposite input of the OR gate (pin 5, 02-3A) receives the positive "comparison period" signal from pin 13, 7473-1B, which will be described in a later paragraph. The hold signal lasts as long as either the EOC or the comparison period signal remains high.

Print/Auto-Reset Pulses

The hold command is connected also to the input of the 74121-3 one-shot. When the hold signal terminates, a one microsecond, positive "print" pulse is produced at the pin 6 output of the one-shot, and a one microsecond, negative "auto-reset" pulse is produced at the pin 1 output. Either the print pulse is admitted through gate 00-2A to the RS latch to set the print command or the auto-reset pulse is admitted through gates 02-2D and 02-3D to reset the processor for the next signal. Which pulse is passed depends

on whether or not the input to the 7473-2B has been clocked, which in turn depends on whether the visibility measurement was rejected or not. If the measurement is rejected, the 7473-2B is clocked and its $\overline{Q}$ output goes low, enabling gate 02-2D to pass the auto-reset pulse to reset the processor. If the measurement is accepted, the 7473-2B is not clocked, its $\overline{Q}$ output remains high, and gate 00-2A is enabled to pass the print pulse to issue a print command.

Rejecting a Visibility Measurement

The visibility measurement will be rejected if a logic 1 is output from either 710-7 or 710-8 of Figure 13, page 68, indicating that the visibility has varied beyond the preselected 5 percent limits, as discussed previously under the heading "visibility variation window," under the signal processing circuit. A measurement will also be rejected if the pedestal exceeds 10 volts at the divider or if the a.c. component exceeds 4.5 volts at the divider (exceeding the linear range of the envelope detector). If either of these limits is exceeded, a logic 1 appears at the output of the 710-3 or 710-4 (Figure 15, page 80) comparators which monitor the corresponding values of the a.c. sig. and the scaled pedestal. A logic 1 appearing at either of these outputs is passed through gate 02-2C to clock the $\overline{Q}$ output of 7473-1A low. (The $\overline{Q}$ output in this case remains low until it is reset by the output of gate 02-1B falling to logic zero after signal passage.)

Gates 02-3C and 00-1C are wired as a 3-input OR gate such that if the visibility varies beyond limits or the pedestal or a.c. component exceeds limits, the output of 00-1C goes to logic 1. This logic 1 will be passed and inverted through gate 00-1D to clock the 7473-2B only if it occurs while this gate is enabled by the positive "comparison period" signal from $\overline{Q}$ of 7473-1B. As described earlier, clocking the 7473-2B results in the processor being automatically reset rather than in a print command being issued.

Comparison Period Signal

The comparison period signal is a positive pulse produced at the $\overline{Q}$ output of the 7473-1B at the time the convert command is given. Its purpose is to maintain the hold signal and enable gate 00-1D for the period of time during which the visibility being output by the divider is compared with the visibility being held and converted. The comparison period pulse is generated when the complement of the convert command (issued from pin 6 of the 9601) resets the 7473-1B $\overline{Q}$ output to a logic 1. The comparison period pulse is terminated when the clock input to the 7473-1B falls and $\overline{Q}$ returns to logic 0.

Termination of the comparison period occurs when the particle, traveling in the y direction, reaches $y_n = 0.4$ (see Chapter III); i.e., when the magnitude of the a.c. component has decreased to $\exp(-2y_n^2) \simeq 0.73$ times its peak

value. The a.c. pk. from the output of op-amp 741-4 in Figure 14, page 75, is fed to the sample-hold module shown in Figure 15, page 80. (This is a model SHM-2, identical to the one in the signal processing circuit already described.) The sample-hold is commanded to hold when the peak of the a.c. passes. The output of the sample-hold is voltage divided to obtain 0.8 times the a.c. pk., which in turn serves as a voltage reference for comparator 710-6. The a.c. sig. is fed to the opposite input of this comparator. When the a.c. sig. has fallen to the referenced 0.8 times the a.c. pk., corresponding to the scaled a.c. being 0.73 times the a.c. pk., the 710-6 output goes to logic 1. This signal, passed and inverted through gate 02-2B, clocks the 7473-1B and terminates the comparison period. The purpose of the sample-hold is simply to reduce voltage droop in the a.c. pk. for the longer period of time it takes for the particle to reach $y_n = 0.4$.

Resetting the Processor

As described earlier, the processor is reenabled by a momentary low being applied to pin 6 of flip-flop 7473-2A. It is also necessary to reset flip-flop 7473-2B, and to reset the RS latch flip-flop to remove the print command if one was issued. Resetting these three flip-flops is accomplished by a negative pulse from the output of gate 02-3D in Figure 15.

When data and a print command are issued to an external recorder, the recorder responds with a "hold-off" command until data transfer is complete. The control circuit requires a positive hold-off signal, which is brought in to pins 3 and 4 of one-shot 74121-2. When the hold-off signal terminates, the 74121-2 produces a 1 microsecond positive pulse which passes through gate 02-3D, resetting the processor.

Alternatively, if no external recorder is attached and the visibility is simply read from the front panel LED display, the processor may be manually reset by momentarily grounding the push-button switch located in the output line of gate 02-3D.

Bench check and processor performance are the subject of Chapter VI.

CHAPTER VI

SIGNAL PROCESSOR: BENCH CHECK

I. LINEARITY AND DIVIDER ERROR

The processor described in the preceding chapter was bench-tested using signal generators. Linearity of the pedestal and a.c. channels was checked by introducing a sine wave at the input to the processor, first at frequencies accepted by the pedestal channel and then at frequencies accepted by the a.c. channel. A Tektronix Model 7904 high frequency oscilloscope with dual channel input permitted simultaneously monitoring the input and the output at various points in the circuit for varying signal amplitudes. The only measurable nonlinearity found was in the a.c. channel envelope detector, whose static response to a 15 MHz sine wave of various constant magnitudes is plotted in Figure 12, page 63. The envelope detector frequency response was then checked at modulating frequencies by modulating the 15 MHz test sine wave at frequencies from d.c. to 10 KHz. No significant difference from the static calibration curve of Figure 12 was noted.

The analog divider performance was first checked statically by using variable d.c. power supplies at the numerator and denominator inputs and a digital voltmeter to monitor the input and output voltages. The divider's

accuracy was next checked with a constant numerator input, but with the denominator varying sinusoidally at 10 KHz from zero to a peak value where the output was recorded, the voltages being monitored by an oscilloscope.

Examples of the divider performance are given in Table II.

The static performance of the combination of the envelope detector and the divider was then checked as follows. A 15 MHz sine wave of constant magnitude K was applied to the input of the processor. At the same time, the pedestal channel was disconnected from the divider and a d.c. voltage D from a variable power supply was applied to the divider's denominator input. An effective processor input visibility was thus created of $V_{in} = K/(D/A)$ where A is the pedestal channel gain. For several values of K, the denominator voltage D was varied to create different input visibilities against which the visibilities output by the divider could be compared. Figure 16 shows the curves generated. The curves show the visibility output by the divider versus the effective processor input visibility for five different values of the a.c. measured at the divider numerator input. The entire range of a.c. and pedestal values to be encountered is covered, and therefore Figure 16 represents the expected spread of output visibilities versus the input, due to errors in the envelope detector/divider combination. The curves indicate error introduced by this combination is less than about 5 percent.

TABLE II

ANALOG DIVIDER PERFORMANCE

Numerator/ Denominator (Volts)	Output, Static (Volts)	% Error	Output, 10 KHz (Volts)	% Error
0.5/1	5.20	4%	5.20	4%
1/1	10.05	0.5	10.10	1
5/5	10.00	0	10.00	0
10/10	10.00	0	10.00	0
1/1.25	8.15	2	8.15	2
1/1.5	6.81	2	6.90	3
1/2	5.10	2	5.20	4
1/4	2.54	2	2.60	4
1/10	1.005	0.5	1.05	5

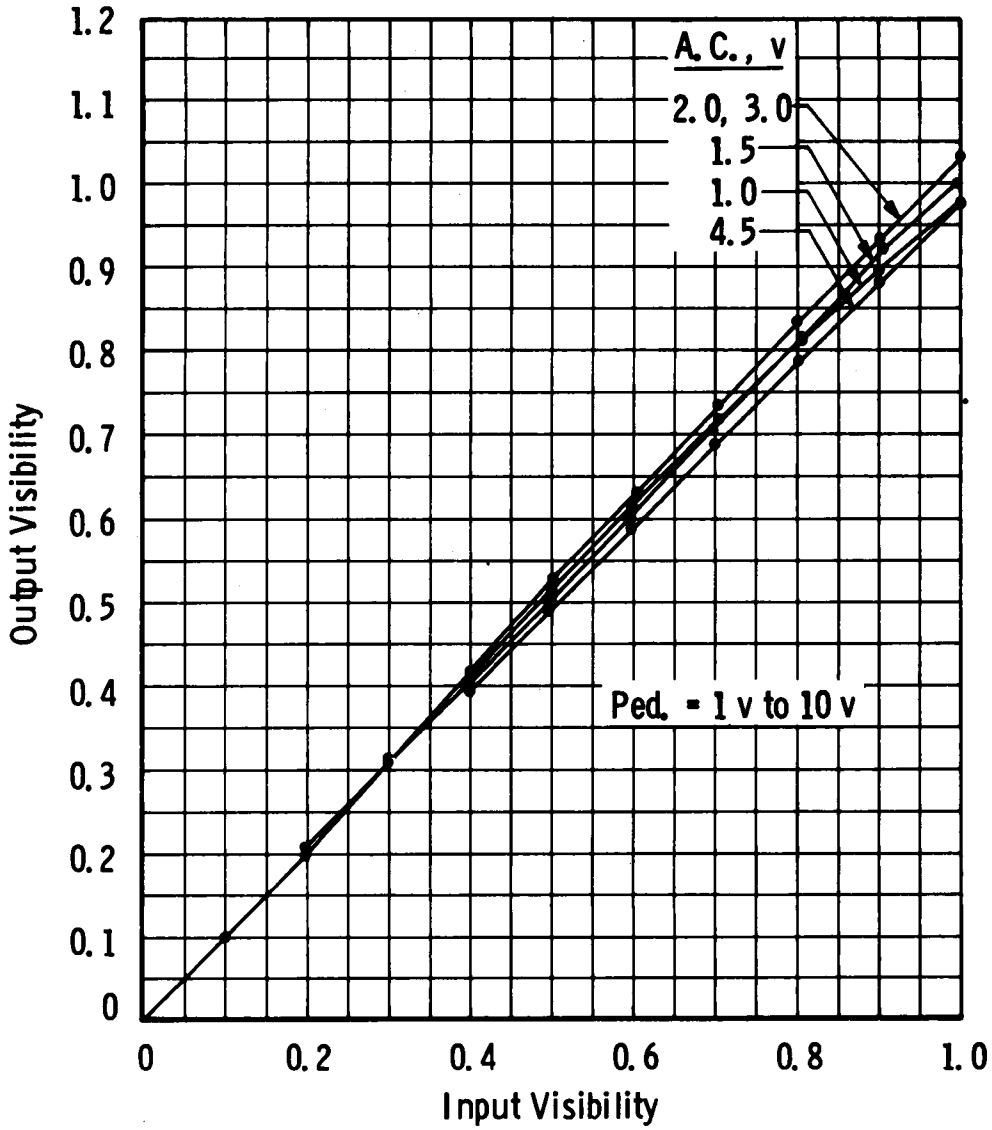


Figure 16. Output versus input visibility for envelope detector/divider combination.

II. EQUALIZING CHANNEL TIME DELAYS

The dual channel input oscilloscope also permitted measuring the time delay through each channel. By applying a 10 KHz sine wave to the processor input and simultaneously displaying both the input and pedestal channel output, the time delay through the channel could be observed. Similarly, by modulating a 15 MHz sine wave carrier at 10 KHz and applying this to the processor input and simultaneously displaying this with the a.c. channel output, the time delay through the a.c. channel could be measured. As reported in Chapter V, the delay through each channel was adjusted to 1.8 microseconds by small screw adjustments of the filter inductors.

III. BIAS STABILITY

Some voltage bias drift occurs in the pedestal channel, which is d.c. coupled throughout. Bias voltage changes with temperature at the output of the uA733-1 first stage amplifier are amplified in the pedestal channel prior to being applied to the denominator input of the divider.

Bias drift in the a.c. channel is less than in the pedestal channel. However, d.c. coupling is used from the base of the 2N3904 at the input to the envelope detector to the numerator input of the divider, and bias changes in this transistor due to temperature variation will be transmitted to the divider.

To eliminate bias drift as a source of error, the a.c. and pedestal channel inputs to the divider are brought out through leads to front panel connectors so that an oscilloscope can be used to monitor bias voltages at these points. The pedestal channel output bias, which should be set to ground potential, is adjustable by a front panel mounted potentiometer (labeled P2 in Figure 11, page 59). This potentiometer varies the bias voltage applied to the noninverting input of the uA715-2 op-amp, which sets the desired pedestal channel bias. The a.c. channel output bias is adjustable by a front panel mounted potentiometer (labeled P1 in Figure 11). This potentiometer varies the bias voltage applied to the base of the envelope detector 2N3904 and should be used to set the bias voltage at the output of the a.c. channel op-amp (uA715-1) to -200 mv. This value was found experimentally to provide optimum envelope detector linearity.

IV. FREQUENCY RESPONSE: SIGNAL CIRCUIT

Frequency response was measured in the a.c. and pedestal channels by varying the frequency of the test input sine wave. Frequency response was determined to be flat ±1 percent over the ranges defined by the signal bandwidths given in Chapter V.

V. FREQUENCY RESPONSE: CONTROL CIRCUIT

Bench testing the control circuit showed that its frequency response is that which limits the maximum particle velocity that will be accepted by the processor. It was found, using a sine wave to simulate the pedestal, that when a particle crosses the probe volume (that is, a distance $2b_0$) in less than 65 microseconds, the signal labeled a.c. pk. at the output of the peak detector (pin 4, 710-1, Figure 14, page 75) develops a high frequency oscillation. This oscillation occurs on the rising side of the signal as it follows the input scaled a.c., and switches the 710-1 comparator, causing an attempted measurement, before the appropriate time at the peak of the waveform. The oscillation was reduced but not eliminated by inclusion of the 100 ohm 2N3904 emitter resistor, and in the present prototype this oscillation limits the maximum permissible particle velocity. For a beam radius b_0 = 500 micrometers, the maximum velocity is 15.4 m/s.

The lower limit on velocity is set by the control circuit peak detector droop. When a simulated signal is applied corresponding to a particle crossing the probe volume in greater than 2 milliseconds, the droop in peak detector output voltage (a.c. pk.) prevents a convert command from being issued at the appropriate time. For b_0 = 500 micrometers, this is a minimum velocity of 0.5 m/s.

VI. DYNAMIC RANGE OF INPUT SIGNAL AMPLITUDES

For a single gain setting, the processor accepts maximum (peak) pedestal voltages over a 10:1 range (1 to 10 volts at the divider input) and maximum (peak) a.c. magnitudes over a 4.5:1 range (1 to 4.5 volts at the divider input). The gain control at the input amplifier (733-1) must be varied to increase this range.

Further flexibility is obtained by using the a.c. gain switch, which has been described in Chapter V. Selecting high a.c. gain boosts a.c. channel gain 2.5 times and simultaneously selects voltage dividing downstream of the divider to compensate. The following examples demonstrate the use of this switch. Voltages shown are peak values reached at the divider input unless otherwise indicated.

1. A.C. gain low:

   Visibility = 1.0

   A.C. range: 1 to 4.5 volts

   Corresponding pedestal range: 1 to 4.5 volts

   Visibility = 0.4

   A.C. range: 1 to 4 volts

   Corresponding pedestal range: 2.5 to 10 volts

2. A.C. gain high:

   Visibility = 0.4

A.C. range: 1 to 4.5 volts (0.4 to 1.8 volt equivalent after divider output is stepped down through voltage divider)

Corresponding pedestal range: 1 to 4.5 volts

Visibility = 0.16

A.C. range: 1 to 4 volts (0.4 to 1.6 volt equivalent after voltage divider)

Corresponding pedestal range: 2.5 to 10 volts

VII. TOTAL GAIN

Total processor gain from input to the divider is greater than 600 with the input amplifier gain set maximum. Since a minimum peak voltage of 1.0 volt is required at the divider input for both the pedestal and a.c. components, both pedestal and a.c. components must peak at at least 1/600 = 1.67 millivolts at the processor input. Further gain is available through the use of a preamplifier at the photodetector output.

VIII. DATA REPETITION RATE

Rapid read-out of accurate size data was the primary goal of this research. The rate at which particles can be sized depends primarily in this instrument on how fast the particles are moving; that is, how long it takes for one particle to move through the probe volume. The minimum time a particle may take to cross the probe volume is about

65 microseconds, as discussed earlier. The analog-to-digital conversion takes only 16 microseconds and is initiated at the peak of the signal. Therefore, provided that the control circuit determines that a measurement is valid, the print command and data are made available to an external recorder before the particle has left the probe volume. The 10 microsecond discharging of the peak detector storage capacitor is completed before or immediately after the particle has left the probe volume. Reset of the processor's flip-flops is accomplished by a 1 microsecond reset pulse after the external recorder's hold-off command terminates to signal that data transfer is complete. Since the minimum time in the probe volume is about 65 microseconds, allowing an extra 10 microseconds for capacitor discharge gives a maximum data repetition rate of about 1/75 = 13.3 KHz, neglecting the external recorder's data transfer rate.

CHAPTER VII

NOISE

Analysis of the noise encountered is facilitated by assuming that the signal at the photodetector output is produced by a stationary particle centered in the probe volume with fringes moving by it. The resultant signal is a cosine wave of constant magnitude (the "a.c." component) added to a constant d.c. voltage (the "pedestal"). As discussed in earlier chapters, if the particle is centered in the probe volume, the ratio of the a.c. magnitude to the pedestal is the visibility V_0.

Noise will appear along with the signal in the photodetector output load resistor. The noise arises primarily from: (1) thermal noise in the load resistor, (2) shot noise in the photodetector output current, and (3) random intensity fluctuations in the laser beam. Noise is also added in the electronic circuit following the load resistor, mostly in the first stage of amplification.

I. THERMAL NOISE AND FIRST STAGE AMPLIFICATION NOISE

Thermal noise is caused by thermal fluctuations of electrons in a resistor. This noise has a two-sided noise voltage power spectral density given by (33):

$$G_{vt}(f) = 2kTR_L \qquad (7\text{-}1)$$

where k is Boltzmann's constant, equal to $1.38(10^{-23})$ joules per degree Kelvin, T is the Kelvin temperature and R_L is the value of the resistance. Since this is a flat spectrum, independent of frequency ("white" noise), the mean-square thermal noise voltage may be written as

$$\overline{v_{nt}^2} = 2B_N G_{vt}(f) = 4kTR_L B_N \qquad (7\text{-}2)$$

where B_N is the noise equivalent bandwidth (33).

Referring to Figure 11, page 59, a thermal noise voltage is developed across the 50 ohm resistor at the pin 14 input to the uA733-1 amplifier. This resistor serves as the load resistor for the photomultiplier tube if no preamplifier is used. In this research, a preamplifier was used, employing a 50 ohm load resistor for the photomultiplier also followed by a uA733 amplifier. Whether a preamplifier then is used in this case or not, analysis of the electronic noise introduced by the load resistor and the first stage of amplification is the same, since the first stage of amplification in both cases is identical. The case where no preamplifier is used is considered here.

The thermal noise due to the load resistor is amplified by the following uA733 and appears at the output of the band pass filter in the a.c. channel and at the output of the low pass filter in the pedestal channel. Additional electronic noise is added by the uA733.

Considering first the pedestal channel, the total noise at the low pass filter output due to the amplified load resistor noise plus the noise from the uA733 may be estimated using specifications supplied with the uA733. The r.m.s. "input noise voltage" (defined as the r.m.s. noise at the 733 output divided by its gain) is specified to be 13 microvolts with a 50 ohm source resistance and a bandwidth of 10 MHz. With an amplifier gain setting of 20 and filter gain of 0.5, this would represent a mean-square noise voltage of $[10(13)10^{-6}]^2 = 169(10^{-10})$ volts^2 at the filter output if the bandwidth were 10 MHz. The mean-square noise voltage is proportional to bandwidth as shown in the equation above, and within the 200 KHz bandwidth of the low pass filter, the mean-square noise may be estimated at $169(10^{-10})\ (0.02) = 3.38(10^{-10})$ volts^2.

This result should be compared with thermal noise generated by, say, the following 1K resistor at the pin 3 input to the uA715-2 op-amp. For this resistor, within the 2 MHz bandwidth of the uA715 (the bandwidth specified for the uA715 for the closed loop gain used) there results:

$$\overline{v_{1K}^2} = 4KTRB_N = 4(1.38)(10^{-23})(300)(10^3)\,2(10^6)$$

$$= 0.332(10^{-10}) \text{ volts}^2$$

which is seen to be an order of magnitude less than the amplified load resistance noise combined with the noise added by the uA733. This illustrates that the significant

electronic noise is contributed by the first amplification stage and the thermal noise of the initial source resistance.

In the a.c. channel, the noise introduced is again essentially that of the amplified load resistor thermal noise and that added by the uA733-1. The bandwidth here, though, is greater than in the pedestal channel. Taking the noise equivalent bandwidth of the band pass filter to be approximately 2 MHz gives a mean-square noise voltage at the filter output of $169(10^{-10})(0.2) = 33.8(10^{-10})$ volts^2.

This noise introduced by the photodetector load resistor and the first amplification stage must now be compared with noise introduced by the other sources mentioned above.

II. PHOTODETECTOR SHOT NOISE

Shot noise due to the discrete nature of charge arises in photoemissive detectors (such as the photomultiplier used in this research) due to the "dark" current which flows in the absence of any illumination. Noise also arises from fluctuations of the incident optical radiation even when the mean radiation intensity is constant (34). This latter noise, due to the signal and background radiation, is often called "photon fluctuation noise," or the "shot noise" due to signal and background radiation.

The anode dark current, specified at typically 5 nanoamperes for the photomultiplier used, is much less than the range of signal currents encountered, and can be

neglected. Stray background radiation can also be minimized, and it will be assumed in the analysis here that the photodetector anode current is that due to the signal alone.

The shot noise due to the signal will be estimated using the following formula for the two-sided current shot noise power spectral density (33):

$$G_{is}(f) = G^2 q I_p \tag{7-3}$$

where G is the current gain of the photomultiplier, q is the electronic charge and I_p is the detector signal current prior to multiplier gain. In order to use this equation, I_p will be taken to be the value of the pedestal, which is the average of the photodetector output current.

The mean-square shot noise current, from the above formula which represents white noise, may be given as

$$\overline{i_{ns}^2} = 2B_N G_{is}(f) = 2B_N G^2 q I_p \tag{7-4}$$

where B_N is the noise equivalent bandwidth. This noise current will produce in a load resistance R_L a mean-square noise voltage of

$$\overline{v_{ns}^2} = 2B_N G^2 q I_p R_L^2 \tag{7-5}$$

To compare this shot noise voltage with the thermal and electronic noise previously discussed, it will be assumed that the average anode current GI_p out of the photomultiplier is 40 microamperes, that $G = 5(10^4)$, $R_L = 50$ ohms

and B_N = 10 MHz, the bandwidth given for the specification of the uA733 input noise voltage. Using these values gives $\overline{v_{ns}^2} = 1.6(10^{-8})$ volts^2, or an r.m.s. value of about 126 microvolts. This is considerably greater than the 13 microvolts specified as input noise voltage for the uA733 amplifier, and it can be concluded that the photodetector shot noise will dominate the thermal and other electronic noise.

Consideration will next be given to what happens to the shot noise in the a.c. channel when it passes through the envelope detector, assuming that there is no laser beam noise; i.e., that the laser output intensity is constant.

The input to the a.c. channel band pass filter has been shown to be predominantly white noise due to the photodetector shot noise. The output of the filter then, is "narrow-band noise," which can be represented as (33, 35):

$$n(t) = n_c(t)\cos \omega_c t - n_s(t)\sin \omega_c t$$

where $\omega_c/2\pi = f_c$ is the center frequency of the band pass filter. The quantities $n_c(t)$ and $n_s(t)$ are statistically independent, Gaussian-distributed, and are relatively slowly varying; each has a power spectral density that resembles low pass filtered white noise of bandwidth one-half that of the band pass filter. Further, the mean-square values of these quantities are related by (35, page 203)

$$\overline{n^2} = \overline{n_c^2} = \overline{n_s^2}$$

Following a derivation in Carlson (35), the signal s(t) plus noise n(t) at the input to the envelope detector may be written for the case here as:

$$s(t) + n(t) = K \cos \omega_c t + [n_c(t)\cos \omega_c t - n_s(t)\sin \omega_c t]$$

where K is constant, remembering the assumption made at the beginning of this noise analysis that the a.c. component is a cosine wave of constant magnitude. The ratio of the r.m.s. noise to the signal envelope K is $(\overline{n^2})^{1/2}/K$.

The signal plus noise may be written alternatively in the envelope-and-phase form

$$s(t) + n(t) = r(t) \cos[\omega_c t + \phi(t)]$$

where

$$r(t) = \{[K + n_c(t)]^2 + [n_s(t)]^2\}^{1/2}$$

$$\phi(t) = \arctan[n_s(t)/(K + n_c(t))]$$

The assumption is made that the signal-to-noise ratio is high, so that the envelope r(t) is approximately

$$r(t) \simeq K + n_c(t)$$

An envelope detector is insensitive to variations in the phase $\phi(t)$ of the signal-plus-noise, and responds only to the envelope. The output, then, is proportional to $K + n_c(t)$ and the ratio of r.m.s. noise to signal in the

output is (providing the detector responds to all the noise frequencies in $n_c(t)$):

$$(\overline{n_c^2})^{1/2}/K$$

But as noted above, $\overline{n_c^2} = \overline{n^2}$, so the ratio of noise to signal is not changed by an envelope detector which passes all the noise frequencies (where the signal well dominates the noise).

In the case under consideration here, the envelope detector does not respond to all the noise frequencies in $n_c(t)$. As mentioned above, $n_c(t)$ has a bandwidth one-half that of the band pass filter; i.e., a bandwidth of approximately 1 MHz. The low pass filter in the envelope detector has a bandwidth of about 200 KHz. The resultant effect is that the envelope detector here affects the noise-to-signal ratio in the channel only by defining the channel bandwidth as the bandwidth of the detector low pass filter.

Shot-Noise-to-Signal Ratios

At the output of the pedestal channel, the mean-square shot noise voltage is A^2 times the mean-square shot noise voltage across the photodetector load resistor in a bandwidth B_N, where A is the voltage gain from the load resistor to the channel output and B_N is the channel bandwidth. From Equation 7-5,

$$A^2\overline{v_{ns}^2} = 2A^2B_NG^2qI_pR_L^2$$

The assumption was made at the beginning of this chapter that the signal is a constant d.c. voltage (the pedestal) plus a cosine wave (the a.c.). The average photomultiplier output current GI_p used in the shot noise expression above is the constant pedestal, giving a pedestal signal voltage GI_pR_L in the load resistor and AGI_pR_L at the channel output. The ratio of r.m.s. shot noise voltage to signal voltage at the pedestal channel output, then, is

$$\frac{\text{noise}_{(\text{rms})}}{\text{pedestal}} = \frac{(2A^2B_NG^2qI_pR_L^2)^{1/2}}{AGI_pR_L} = \left[\frac{2B_Nq}{I_p}\right]^{1/2} \qquad (7\text{-}6)$$

For B_N = 200 KHz, GI_p = 40 microamperes and $G = 5(10^4)$, this ratio is equal to 0.00894; i.e., about 0.9 percent. At the output of the a.c. channel, the shot noise due to the average current GI_p is given by the same expression as above:

$$A^2\overline{v_{ns}^2} = 2A^2B_NG^2qI_pR_L^2$$

where B_N is again 200 KHz. The signal is the cosine wave magnitude, $AV_0(GI_pR_L)$; i.e., the visibility times the pedestal, multiplied by the gain. The ratio of r.m.s. shot noise to the signal is

$$\frac{\text{noise}_{(\text{rms})}}{\text{a.c. component}} = \frac{1}{V_0}\left[\frac{2B_Nq}{I_p}\right]^{1/2} \qquad (7\text{-}7)$$

This is the same ratio as for the pedestal channel except for the inverse proportionality to the visibility. Stated another way, the noise is the same at both channel outputs, but the a.c. signal is proportional to the visibility.

For a low visibility signal where $V_0 = 0.2$, and for the same conditions as given in the above pedestal example, the above formula gives a noise-to-signal ratio of about 4.5 percent.

III. LASER FLUCTUATION NOISE

Two different light sources were tested for this research, a helium-cadmium laser operating at a wavelength of 0.4416 micrometers with an output of 50 milliwatts, and a helium-neon laser operating at 0.6328 micrometers with an output of 3 milliwatts. The helium-cadmium laser was the noisier of the two, and its higher output power was found unnecessary, so the experimental results reported in Chapter VIII were obtained using the lower power and quieter helium-neon source.

Specifications supplied with the noisier helium-cadmium laser state that beam amplitude noise is less than 6 percent r.m.s. from 1 KHz to 100 KHz. Such intensity variations are a multiplicative noise; i.e., they amplitude modulate the a.c. component of the scattered light waveform and appear also in the pedestal. Although this is a relatively low-frequency noise, because it amplitude modulates the a.c. it will be passed by the a.c. channel

band pass filter designed to block the pedestal and low frequency additive noise. This noise can be expected to appear, then, at the a.c. envelope detector output as well as at the pedestal channel output.

The specified 6 percent r.m.s. value compared to the signal is greater than any noise value discussed thus far. Only the shot noise-to-signal ratio in the a.c. channel with a low signal visibility is comparable. At least for the noisier laser, then, noise observed on the signal in either the pedestal or a.c. channels (at high visibilities) will be largely this laser intensity fluctuation noise.

This noise will in theory be cancelled out in the analog divider. If this multiplicative noise is represented by $n_f(t)$, the divider output (neglecting the shot noise) will be proportional to:

$$\frac{n_f(t) \times (\text{a.c. envelope})}{n_f(t) \times (\text{pedestal})}$$

IV. SUMMARY

It has been shown that in the absence of laser intensity fluctuation noise, the dominant noise in the system will be the photodetector shot noise, since it is much greater than the thermal and other electronic noise. In the system used in this research, however, laser beam noise is greater in many cases than the shot noise. The signal-to-noise ratio should be improved beyond the analog

divider in these cases due to the canceling of the laser beam noise in the divider. Oscilloscope photographs of the noise actually encountered are included in Chapter VIII.

CHAPTER VIII

EXPERIMENTAL RESULTS

I. EXAMINATION OF INTENSITY DISTRIBUTION IN PROBE VOLUME

The optical system used is outlined in Figure 1, page 9. The light source was a helium-neon, 3 milliwatt laser operating at a wavelength of 0.6328 micrometers. A Bragg cell beam splitter driven at 15.0 megahertz produced moving fringes in the crossover region of the two beams. A 6-inch diameter, F/5 collection lens was located on axis. The collected light was directed to the photodetector, an RCA type 931A photomultiplier (PM) tube.

The photodetector was followed by a 50 ohm load resistor and an electronic preamplifier consisting of a type uA733 integrated circuit wide-band amplifier. The signal was then fed to the visibility processor described in the preceding chapters.

The beam separation angle α was measured by moving the collection optics aside and allowing the two beams to project onto a far wall. The angle was measured as the ratio of the distance between the beams at the wall to the distance from the wall to the beam crossover point. Since angles used were less than a degree, this method was quite accurate. The fringe spacing was then calculated from the relationship $\delta = \lambda/(2 \sin(\alpha/2))$ (see Equation 2-2).

The illuminating intensity distribution in the probe volume is discussed in Chapter II. It is given by Equation 2-2 and is sketched in Figure 3, page 14. It is possible to examine this intensity distribution experimentally by placing a thin wire in the probe volume. The wire diameter must be much less than a fringe spacing and be oriented parallel to the x-axis. The intensity of the collected light scattered from the thin wire will then be closely proportional to the incident intensity at the location of the wire.

To examine the probe volume, a wire of diameter 10 micrometers was stretched across an aperture and placed vertically (the x-direction) in the region of beam cross-over. The mount for the wire and holder was placed on a traverse system which permitted a positional accuracy of ±1.0 micrometer in the y-direction.

With the wire stationary in the probe volume, the resultant PM tube signal is a continuous wave (CW) oscillation (the "a.c." component) added to a constant d.c. voltage (the "pedestal"). The signal results from the fringes moving by the wire. The visibility is defined (see Chapter II) as the a.c. magnitude divided by the pedestal.

The wire and mount could be pushed by hand smoothly and rapidly through the probe volume. Figure 17a, b and c shows oscilloscope photographs of the resulting PM tube output waveform. The wire was moved in the y-direction through the probe volume at z_n = 0, 0.2 and 0.6, respectively, for

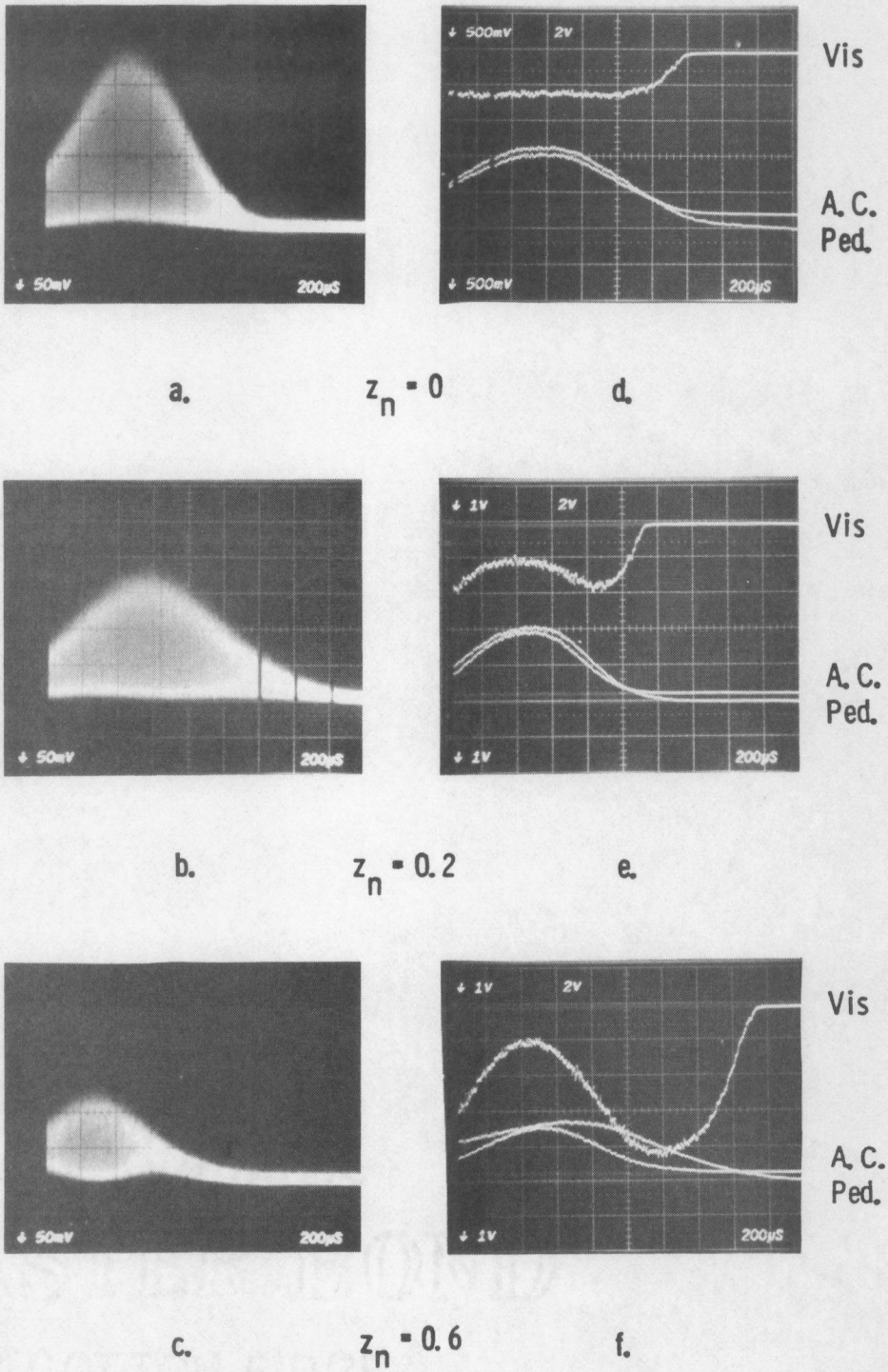


Figure 17. Scattered light and processor waveforms for three values of z_n.

the photographs. (The normalized coordinate z_n is defined in Chapter III; $z_n = 0.2$, for example, refers to that z coordinate 0.2 of the way to the edge of the probe volume from probe center.) The individual a.c. cycles are not discernable in the photographs, since the period of a.c. oscillation is very short compared to the time required for the wire to pass through the probe volume. (Figure 17, for example, should be compared with Figure 4, page 17, which represents a waveform where the fringes are stationary.) Visibility is near 1.0 in each photograph at probe center.

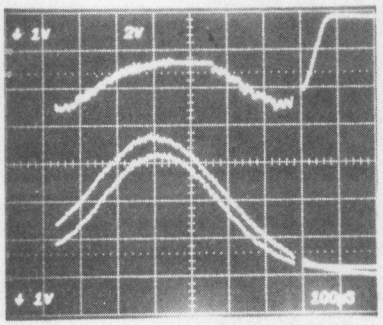
Photographs of corresponding waveforms within the signal processor are shown in Figure 17d, e and f. The top trace in each figure is the visibility (monitored at the analog divider output). Zero reference for the visibility trace is the next-to-bottom reference line and the scope voltage sensitivity was set at 2 volts per division. In each figure, a visibility of close to 1.0 (10 volts) is indicated at probe center. The analog divider output between waveforms rests at nearly 12 volts. (This was discussed in Chapter V.) The a.c. magnitude and pedestal, monitored at the analog divider inputs, are shown in the lower two traces. Zero reference for both these two traces is the second reference line up from the bottom. (A greater scope voltage sensitivity is shown on the photograph for $z_n = 0$, because a lower PM tube gain was used for this case.) The pedestal bias lies at zero volts between waveforms and the a.c. bias rests at 200 millivolts, the value

found to give best envelope detector linearity, as discussed in Chapter V.

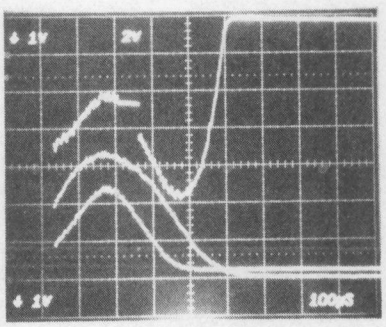
Figure 17d, e and f, page 114, clearly shows that the visibility remains approximately constant throughout the waveform at $z_n = 0$, but for other values of z_n, falls off as the particle leaves the probe volume in accordance with Equation 4-2, page 50.

II. TESTING CONTROL CIRCUIT OPERATION

Figure 18a and b demonstrates the operation of the processor control circuit. The oscilloscope traces shown are the same as in Figure 17d, e and f, except the visibility trace (top) is monitored just downstream of the track/hold module shown in Figure 9, page 44 (and the zero references on the scope have been changed). In Figure 18a the particle passed near $z_n = 0$ and the visibility varied a relatively small amount during traversal. At the peak of the a.c. signal, the track/hold was given the command to hold, and it remained in hold for the time that the visibility is shown as a short, constant line. The visibility output by the divider did not vary much during this time and the held value, converted to digital form, was accepted as a valid measurement and was transmitted to the processor output and LED display. Figure 18b, on the other hand, shows a case where a particle passed some distance from $z_n = 0$, and the visibility rapidly dropped off as the particle left the probe volume. The short, constant line shows the comparison



a. Measurement accepted;
processor read out vis = 0.905.



b. Measurement rejected.

Figure 18. Control circuit operation.

period when the held value was compared with the subsequent output of the divider. When the track/hold was returned to "Track" at the end of the comparison period, the amount of immediate change on the trace shows how much the divider output had changed. The measurement was rejected by the processor in this case.

III. TESTING PROCESSOR ACCURACY OF VISIBILITY MEASUREMENT

Simultaneous photographs were taken of the processor input waveform and the visibility output by the track/hold module to confirm the accuracy of visibility measurement by the processor. In this test, particles were blown through the probe volume which were either naturally occurring room dust particles, blown by an electric fan, or glass test spheres blown by a dry nitrogen jet. The actual size of the particles was not of interest here; only the visibility of the scattered light waveform was of concern.

Figure 19 shows a sample of the photographs taken. In each of these photographs, the measurement was accepted and output by the processor. Visibility was measured by hand directly from the photographs of the input waveforms for comparison with the processor output in each case. For measurement of the input waveform, the visibility was obtained from the relationship

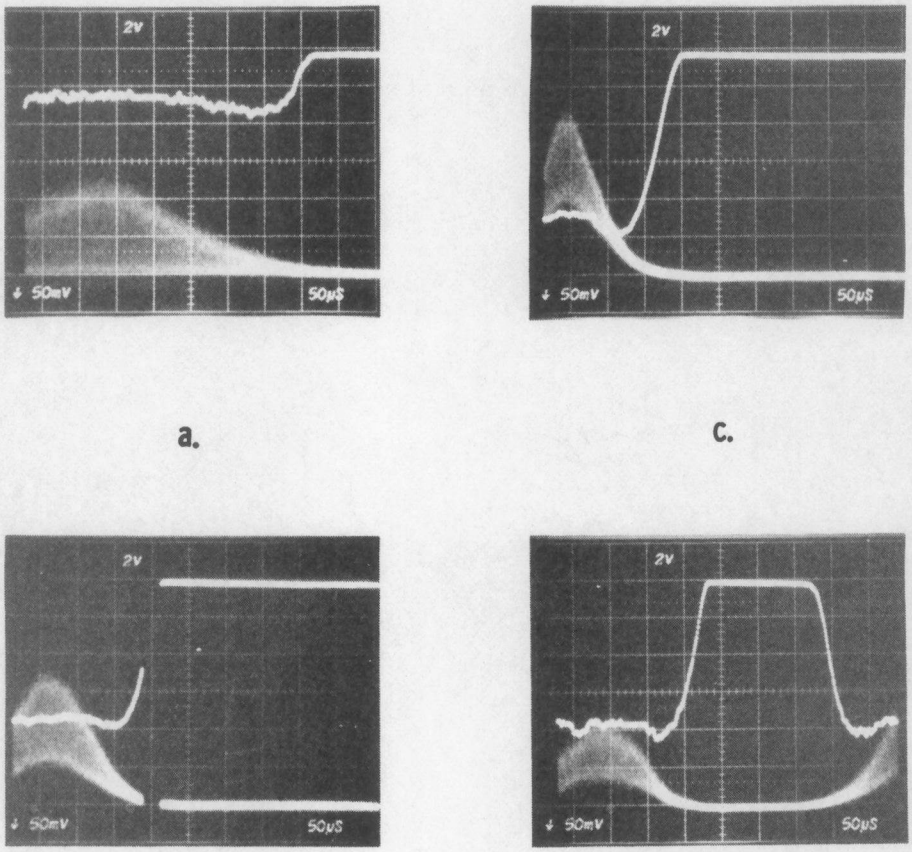


Figure 19. Scattered light waveforms and corresponding processor output visibility.

$$V = \frac{\text{a.c. magnitude}}{\text{pedestal}} = \frac{(I_{mx} - I_{mn})/2}{(I_{mx} + I_{mn})/2}$$

where I_{mx} is the maximum value reached by the waveform at probe center and I_{mn} is the minimum value of the waveform at probe center.

For example, for the photographs of Figure 19, the following was obtained.

Figure	Measured Input Visibility	Processor Output (LED Display)
19a	0.87	.910
19b	0.43	.434
19c	0.30	.307
19d	0.39	.405

(In Figure 19d, a second particle may be seen entering the probe volume following visibility measurement of the first.)

Figure 20 plots data for 69 such photographs. The abscissa represents visibilities measured by hand from the input waveform. The ordinate gives the corresponding processor output. This plot of data may be compared with Figure 16, page 93, which shows divider output versus processor input for various values of a.c. and pedestal, measured during bench check of the processor. The "outside" lines of Figure 16 are redrawn as the solid lines in Figure 20. They represent limits within which errors in visibility measurement could be explained by nonlinearities in the envelope detector and divider. The dashed lines on

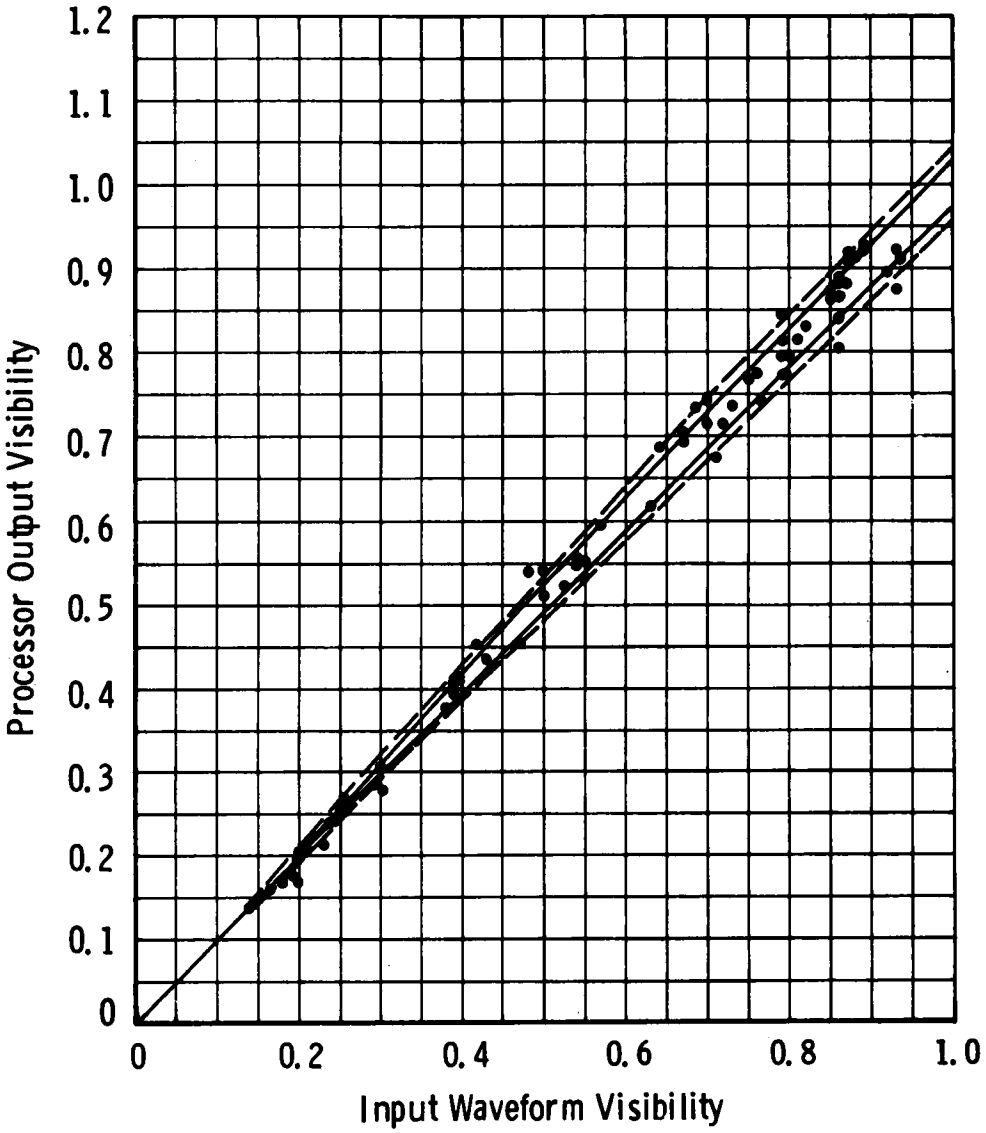
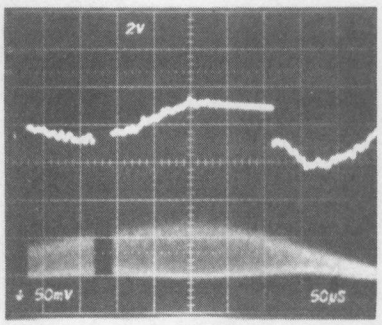


Figure 20. Processor output visibility versus input waveform visibility.

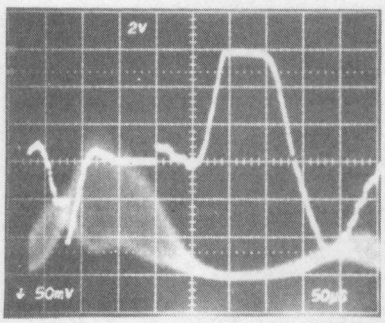
Figure 20 are drawn a distance outside the solid lines which represents approximately two standard deviations (2σ) of noise existing on the output visibility. (This noise was estimated from photographs included in the last section of this chapter.) Errors in the data points falling within the dashed lines, then, could be explained by nonlinearities in the envelope detector/divider combination, plus noise.

Some data points still fall outside the dashed lines, showing some error exists from other sources. There is, of course, some error in measuring the input visibility on the photographed waveforms; it cannot be assumed that the actual visibility has been determined by hand without error. Further error can be attributed to such sources as small instrument nonlinearities not included in the plots of Figure 16, page 93, small nonuniformity of frequency response over the applicable ranges and noise excursions greater than 2σ.

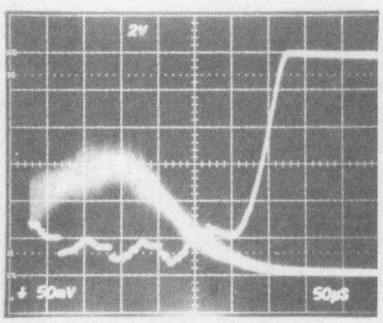
The ability of the processor to reject unwanted waveforms is shown in Figure 21. Figure 21a shows the input waveform and output visibility for a particle which did not pass through the center of the probe volume. It is a case of the sort discussed previously, and the measurement was rejected. (The short blank area occurring in both traces in this picture was introduced by the oscilloscope.) Figure 21b and c appears to show waveforms resulting from more than one particle in the probe volume at a time. In Figure 21b, a falling a.c. magnitude twice initiated an attempt at



a.



b.



c.

Figure 21. Waveforms rejected by processor.

measurement, and in Figure 21c, three attempts were made. In all five cases, the visibility was rapidly changing, and the measurements were rejected.

IV. VISIBILITY MEASUREMENT FOR SPHERES OF KNOWN SIZE

Batches of glass beads were available for test. The batches were specified by the manufacturer to contain 90 percent true spheres, with 98 percent of the beads in the specified size range. Observation of samples of these beads on a glass slide with a microscope indicated many spheres within the size range, but also a number of particles in each batch which were not spherical and were not of the size specified. Samples of these batches were blown through the probe volume for visibility measurement using a jet of dry nitrogen.

In the first test, the fringe spacing δ was measured to be 148 micrometers. By moving a thin wire through the probe volume and observing the position of the wire indicated by the traverse system and the corresponding scattered light waveform, the diameter $2b_0$ of the probe volume was determined to be 340 micrometers. The largest particles looked at were in the size range 44 to 53 micrometers, and therefore the probe diameter was more than six times larger than the largest particles. Although this does not fully satisfy the requirement given in Chapter II that the particles be much smaller than the probe volume, computer

analysis of the average intensity incident on the particle in this case indicated that not much variation from the theoretical visibility should be expected. Visibility was measured for roughly 100 beads from each of two batches. The mean visibility and standard deviation were calculated. Results of this test are as follows:

Specified Diameter D	D/δ	Mean D/δ	Mean Measured Visibility	Standard Deviation
44-53 μm	.30-.36	.33	.69	.04
37-44 μm	.25-.30	.275	.72	.05

The mean measured visibilities fall about 20 percent below what would be expected from the "Fringe Model" curve of Figure 5, page 23.

The fringe spacing δ was then changed and measured to be 59 micrometers. The new probe diameter $2b_0$ was measured to be 400 micrometers. Further visibility data runs were taken for three batches, with specified sizes of 15-37, 37-44 and 44-53 micrometers. The data were scattered but pointed to visibilities much lower than expected.

To confirm that the visibilities being measured did not agree with the fringe model prediction, several glass spheres were placed on a glass slide and their diameters measured with a microscope and calibrated reticle. The spheres were then inserted on the slide into the probe volume, and their visibilities were measured from the wave-form appearing at the output of the PM tube. Results are

shown in Table III. The measured visibilities are all much less than would be expected and led to the investigation of Fraunhofer diffraction to find a more accurate description of the scattered light signal.

The data points obtained for the individual glass spheres (δ = 59 μm) and for the samples with narrow, specified size distributions measured with δ = 148 μm are plotted in Figure 22. The theoretical curves of Figure 5, page 23, are also shown. Although at the present time data are inconclusive, the Fraunhofer diffraction curve offers a better explanation of the visibilities measured, especially the increasing visibilities for D/δ = .730 and .763.

V. NOISE

Examples of the noise in the a.c. and pedestal channels and in the visibility output of the analog divider are shown in the photographs of Figure 23. For the photographs, a stationary wire was placed in the probe volume, creating a constant signal in the a.c. and pedestal channels and at the output of the divider. The visibility could be varied by rotating the wire through a small angle with respect to the fringe planes.

The three traces in each photograph represent, from top to bottom, the visibility output by the divider, the pedestal channel output and the a.c. channel output respectively. The oscilloscope was used in the "chop" mode, sampling each voltage one after the other and repeating this

TABLE III

EXPERIMENTALLY MEASURED VISIBILITY OF GLASS SPHERES

Diameter	D/δ	Measured Visibility
28 μm	.475	.37
30	.509	.32
35	.593	< .04
43	.730	.09
45	.763	.15

δ = 59 micrometers

$2b_0$ = 400 micrometers

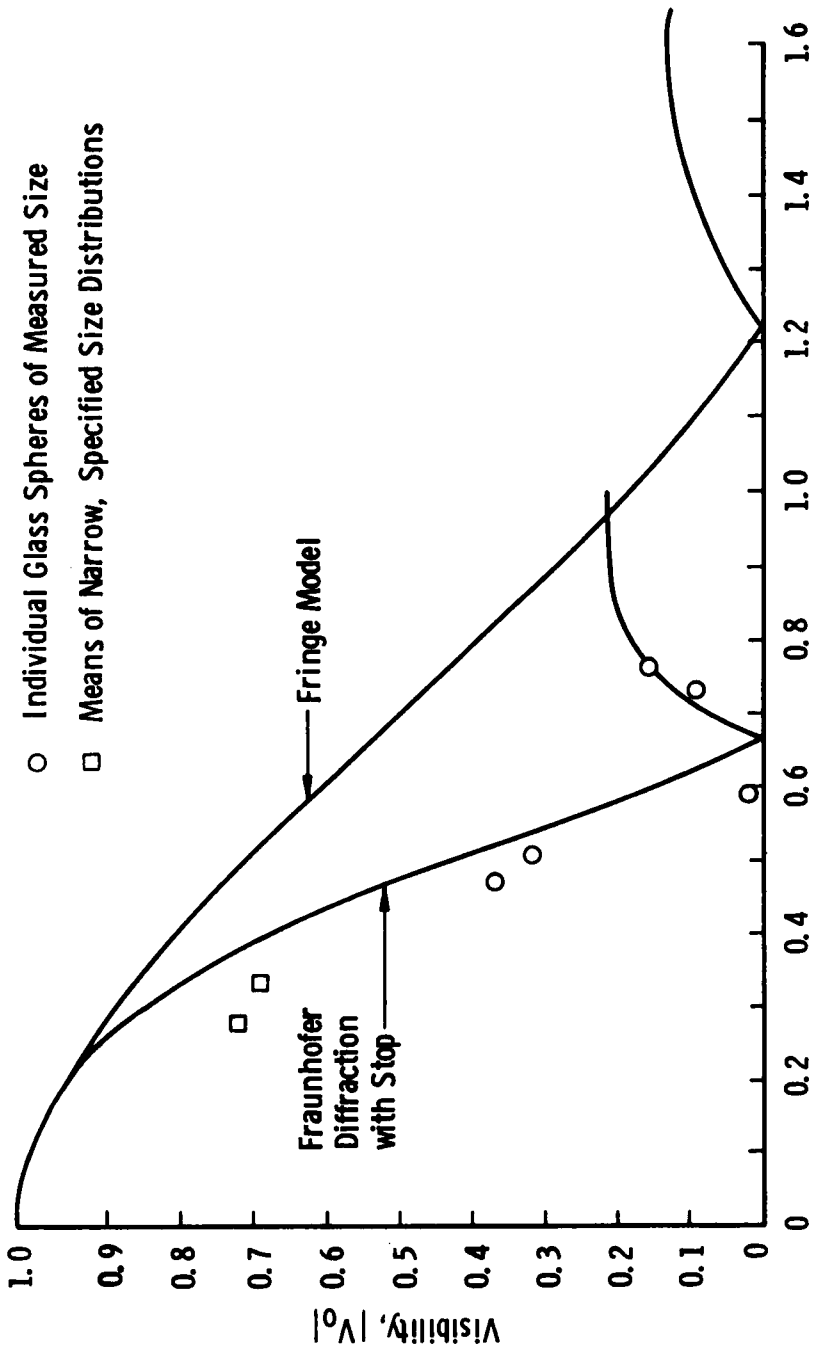
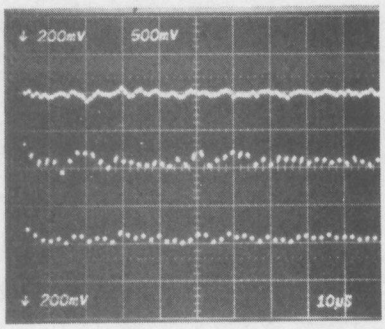
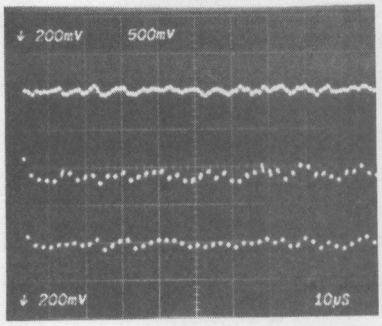


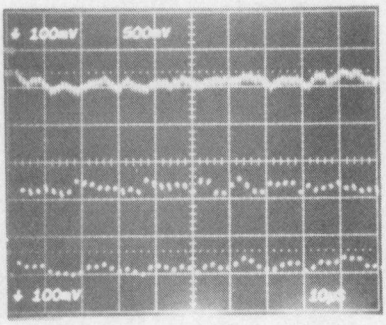
Figure 22. Theoretical visibility curves and experimental data.

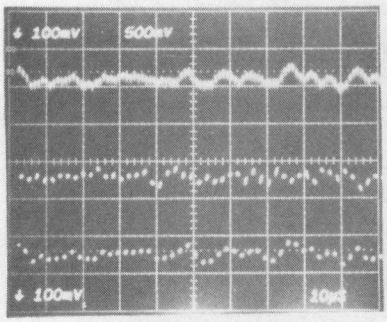




{Vis = 6.7 v*
(7.5%/div) **
{Ped. = 6.0 v
(3.3%/div)
{A. C. = 4.0 v
(5.0%/div)

a.



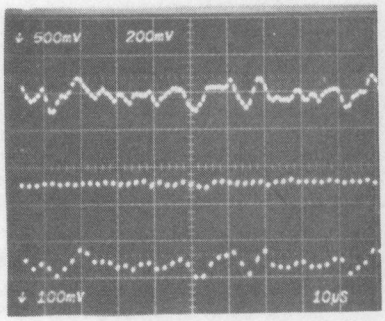


{Vis = 7.1 v
(7.0%/div)
{Ped. = 2.1 v
(4.8%/div)
{A. C. = 1.5 v
(6.7%/div)

b.

*Mean value

**Scope voltage sensitivity, percent of the mean value per division



{Vis = 1.8 v
(11.1%/div)
{Ped. = 5.5 v
(9.1%/div)
{A. C. = 1.0 v
(10%/div)

c.

Figure 23. Noise on visibility, pedestal and a.c. signals.

during the sweep across the screen so that the three traces are simultaneous. The time base for each photograph displayed at the bottom right of the screen is 10 microseconds per division, so that each sample of traces is visible for 100 microseconds.

The zero reference voltage for each trace is below the bottom of the screen and is different for each trace. The scope voltage sensitivity (volts per division) is displayed on the screen and may be different for the three traces. (The sensitivity for the top trace is shown to the right, and the sensitivity for the middle and bottom traces is shown to the left, at the top and at the bottom of the screen, respectively.)

In Figure 23a, the mean visibility voltage is about 6.7 volts (representing a visibility of 0.67), the pedestal mean is about 6 volts and the a.c. mean is about 4 volts. The noise voltage excursions about these means can be estimated as a percentage of the mean in each case by noting the sensitivity per division with respect to the mean value given above. For example, for the visibility of Figure 23a, one division represents about 7.5 percent of the mean; for the pedestal, one division represents about 3.3 percent of the mean; and for the a.c., one division represents about 5.0 percent of the mean.

No attempt was made to make a quantitative measurement of the noise powers involved here. A rigorous theoretical and experimental study of the noise on dual-scatter

velocimeter signals is not within the scope of this work. Some qualitative observations may be made, however.

The noise excursions are in qualitative agreement with the theoretical noise predictions of Chapter VII. The noise excursions in Figure 23a, page 129, at a relatively high visibility and pedestal, for example, are seen to be about 1 percent of the mean, indicating an r.m.s. noise-to-signal ratio on the order of 1 percent. The percentage noise in Figure 23b has increased somewhat with the decreased pedestal (visibility approximately the same). In Figure 23c, at a low visibility, the percentage noise has considerably increased in the a.c. channel while remaining low in the pedestal channel.

In Figure 23a, with the relatively high visibility and pedestal, considerable correlation seems evident between the noise excursions in the bottom two traces, representing the a.c. and the pedestal. This correlation would be due to laser beam amplitude fluctuation, which is passed by both channels. As discussed in Chapter VII, this noise should tend to cancel in the divider, and these photographs bear this out.

In Figure 23b, correlation between a.c. and pedestal noise is less evident, with the increased shot noise masking the beam fluctuation noise.

Finally, in Figure 23c, at a low visibility, no correlation is evident between pedestal and a.c. traces, as the noise in the a.c. channel is predominantly shot noise.

On the other hand, since percentage noise on the pedestal is low and noise on the a.c. is high, it can be seen that the a.c. noise excursions are simply passed on to the visibility in the top trace.

CHAPTER IX

CONCLUSIONS

The primary goal of the research reported here was to examine the theory of interferometric particle sizing with respect to electronic capabilities, in order to design and build an electronic processor for rapid, on-line read-out of size data. The theory relating the visibility of the scattered light waveform to the scattering particle diameter was reviewed. The variation of the visibility with the particle's passage through the probe volume was examined to see what electronic method could best be used to give accurate visibility measurement. The time-varying signals involved (pedestal, a.c. and visibility) were analyzed in the frequency domain to determine required bandwidths.

An electronic processor for visibility measurement was then designed, fabricated and bench-tested. Error in visibility measurement indicated by bench-testing was approximately 5 percent or less.

The processor was then interfaced with the optics of a dual-scatter laser velocimeter. Results of testing with real signals demonstrated that the processor is capable of visibility measurement within the accuracy predicted by bench-testing. The capability of the processor to reject unwanted signals was also demonstrated.

The measured visibility of spherical particles of known diameter, however, did not agree with that predicted by the existing theory. This prompted a derivation of the relation of visibility to size using scalar diffraction theory. This approach was found to give a size versus visibility relationship which better explains the data obtained here.

It is recommended that an extensive theoretical and experimental investigation be undertaken to define under all conditions the relationship that exists between visibility and particle diameter. The effects, if any, of refracted and reflected light on the visibility should be included, or else conditions should be defined where reflected and refracted light will not bias the measured visibility.

The visibility function, given by Equation 2-7, page 21, contains information about the particle's traversal of the probe volume beyond information regarding size. The shape of this function as it varies with coordinates y and z was described in Chapter III as two long levees, or dikes, lying along the x and y axes, intersecting at the origin. The slope of the sides of the levees increases with distance from the origin. The height of the levees is everywhere V_0, through which the visibility is related to size. The electronics described here can read out continuously the value of the visibility as a particle of given size moves through the interference fringe set, and the possibilities should be explored of using the visibility to obtain such

information as where and in what direction the particle passed through the probe volume, its velocity, etc.

Attention can also be turned to an improved design for the electronic instrumentation. Regarding the processor whose design is described here, several areas may be improved as follows:

1. The dynamic range of acceptable signal amplitudes should be increased, which is presently limited to about a 10:1 range by the envelope detector and analog divider.
2. Drift of the pedestal bias voltage should be reduced. In the present processor, the pedestal bias requires close monitoring with an oscilloscope during the taking of data to insure that it is kept at ground potential.
3. Linearity of the 15 MHz a.c. envelope detector should be improved. Its ±5 percent nonlinearity is the greatest single source of error in the processor. Linearity could probably be improved by designing the system for a lower a.c. frequency, say 5 MHz.
4. The frequency response of the control circuit should be improved to respond to particles moving with higher velocities. For a laser beam waist radius b_0 = 500 micrometers, present maximum particle velocity is about 15 meters per second.

A final observation regarding the present processor is that testing with real signals produced higher data rates for the smaller particles with higher visibilities, indicating that the control circuit may "prefer" the higher visibilities with attendant higher signal-to-noise ratios. The effect of this possible bias should be examined when it is desired to obtain size distributions.

BIBLIOGRAPHY

BIBLIOGRAPHY

1. Brayton, D. B. "Small Particle Signal Characteristics of a Dual-Scatter Laser Velocimeter," Applied Optics, 13:2346-2351, October, 1974.

2. Brayton, D. B., and W. H. Goethert. "A New Dual-Scatter Laser Doppler-Shift Velocity Measuring Technique," ISA Transactions, 10:40-50, 1971.

3. Rudd, M. J. "A New Theoretical Model for the Laser Dopplermeter," Journal of Physics E, 2:55-58, January, 1969.

4. Penny, C. M. "Differential Doppler Velocity Measurements," IEEE Journal of Quantum Electronics, QE5: 318, June, 1969.

5. Durst, F., and J. H. Whitelaw. "Optimization of Optical Anemometers," Proceedings of the Royal Society of London, 324(Series A):157-181, August, 1971.

6. Lennert, A. E., D. B. Brayton, and F. L. Crosswy. "Summary Report of the Development of a Laser Velocimeter to Be Used in AEDC Wind Tunnels," Arnold Engineering Development Center TR-70-101, Arnold Air Force Station, Tennessee, July, 1970.

7. Durst, F. "Scattering Phenomena and Their Application in Optical Anemometry," Journal of Applied Mathematics and Physics, (ZAMP), 24:619-643, 1973.

8. Mayo, W. T. "Simplified Laser Doppler Velocimeter Optics," Journal of Physics E, 3:235-237, March, 1970.

9. Farmer, W. M. "The Interferometric Observation of Dynamic Particle Size, Velocity, and Number Density." Ph.D. dissertation, The University of Tennessee, Knoxville, 1973.

10. Farmer, W. M. "Measurement of Particle Size, Number Density, and Velocity Using a Laser Interferometer," Applied Optics, 11:2603-2612, November, 1972.

11. Van de Hulst, H. C. Light Scattering by Small Particles. New York: John Wiley and Sons, Inc., 1957.

12. Kerker, M. The Scattering of Light and Other Electromagnetic Radiation. New York: Academic Press, Inc., 1969.

13. Phillips, D. T., and P. J. Wyatt. "Single-Particle Light-Scattering Measurement: Photochemical Aerosols and Atmospheric Particulates," Applied Optics, 11:2082-2087, September, 1972.

14. Blau, H. H., Jr., D. J. McCleese, and D. Watson. "Scattering by Individual Transparent Spheres," Applied Optics, 9:2522-2528, November, 1970.

15. Hodkinson, J. R., and J. R. Greenfield. "Response Calculations for Light-Scattering Aerosol Counters and Photometers," Applied Optics, 4:1463-1474, November, 1965.

16. Blau, H. H., M. L. Cohen, L. B. Lapson, P. von Thuna, R. T. Ryan, and D. Watson. "A Prototype Cloud Physics Laser Nephelometer," Applied Optics, 9:1798-1803, August, 1970.

17. Moroz, W. J., V. D. Withstandley, and G. W. Anderson. "A Portable Counter and Size Analyzer for Airborne Dust," The Review of Scientific Instruments, 41: 978-983, July, 1970.

18. Watanabe, Y. "Design Consideration of the Prototype Particulate Instrumentation by Laser Light Scattering (PILLS III) System." Ph.D. dissertation, The University of Tennessee, Knoxville, 1973.

19. Cornillault, J. "Particle Size Analyzer," Applied Optics, 11:265-268, February, 1972.

20. Livesey, P. J., and F. W. Billmeyer, Jr. "Particle Size Determination by Low-Angle Light Scattering: New Instrumentation and a Rapid Method of Interpreting Data," Journal of Colloid and Interface Science, 30:447-472, August, 1969.

21. Hodkinson, J. R. "Particle Sizing by Means of the Forward Scattering Lobe," Applied Optics, 5:839-844, May, 1966.

22. Knollenberg, R. G. "The Optical Array: An Alternative to Scattering or Extinction for Airborne Particle Size Determination," Journal of Applied Meteorology, 9:86-103, February, 1970.

23. Bentley, H. T. "Fiber Optics Particle-Sizing System," Arnold Engineering Development Center TR-73-111, Arnold Air Force Station, Tennessee, September, 1973.

24. Trolinger, J. D., and R. A. Belz. "Holography in Dust Erosion Facilities," Arnold Engineering Development Center TR-73-160, Arnold Air Force Station, Tennessee, September, 1973.

25. Belz, R. A., and N. S. Dougherty, Jr. "In-Line Holography of Reacting Liquid Sprays," Proceedings of the Engineering Applications of Holography Symposium. Redondo Beach, California: Society of Photo-Optical Instrumentation Engineers, 1972. Pp. 209-218.

26. Stigliani, D. J., Jr., R. Mittra, and R. G. Semonin. "Particle Size Measurement Using Forward-Scatter Holography," Journal of the Optical Society of America, 60:1059-1067, August, 1970.

27. Adler, R. "Interaction Between Light and Sound," IEEE Spectrum, 4:42-54, May, 1967.

28. Crosswy, F. L., and J. O. Hornkohl. "Signal Conditioning Electronics for a Laser Vector Velocimeter," The Review of Scientific Instruments, 44:1324-1332, September, 1973.

29. Goodman, J. W. Introduction to Fourier Optics. New York: McGraw-Hill Book Company, Inc., 1968.

30. Born, M., and E. Wolf. Principles of Optics. New York: Pergamon Press, Inc., 1965.

31. Gradshtein, I. S., and I. M. Ryzhik. Table of Integrals, Series and Products. New York: Academic Press, Inc., 1965.

32. Van Valkenburg, M. E. Network Analysis. Englewood Cliffs, New Jersey: Prentice Hall, Inc., 1955.

33. Schwartz, M. Information Transmission, Modulation, and Noise. Second edition. New York: McGraw-Hill Book Company, Inc., 1970.

34. Pratt, W. K. Laser Communication Systems. New York: John Wiley and Sons, Inc., 1969.

35. Carlson, A. B. Communication Systems. New York: McGraw-Hill Book Company, Inc., 1968.

VITA

Donald W. Roberds was born February 6, 1933 in Fayetteville, Arkansas, where his father taught physics at the University of Arkansas. He attended grade schools there and in Collingswood, New Jersey and Fort Worth, Texas, and graduated from Venice, California High School in 1950.

He attended the University of California at Los Angeles and the University of Kansas, graduating in 1955 with an A.B. degree in Physics.

Having received an Air Force commission through the Reserve Officers' Training Corps, he attended Air Force flying training in Florida. He left the Air Force as a Major in 1970, having served as a B-47 bomber aircraft commander, as a T-39 pilot and aircraft maintenance officer in England, and as a forward air controller in Vietnam.

He received the Master of Science degree in Electrical Engineering in 1965 from the University of Kansas, through the Air Force Institute of Technology program.

He is married to the former Helen Louise Buck of Fullerton, California. They have one son, David, who was born in 1964. In 1970 the author and his family moved to Tullahoma, Tennessee where he began work at The University of Tennessee Space Institute toward his doctorate. He is now employed as a Research Engineer with ARO, Inc.